ARTICLE

Genesis and timing of Mo mineralization in the Mada Ring Complex, north-central Nigeria: insights from whole-rock geochemistry, Nd-Sr isotopes, zircon U-Pb-Hf isotopes, and molybdenite Re-Os systematics

Musa Bala Girei [1,2,3] · Huan Li [2] · Victor Ikechukwu Vincent [1] · Thomas J. Algeo [1,4,5] · Safiyanu Muhammad Elatikpo [2,6] · Saleh Ibrahim Bute [7] · Hafizullah Abba Ahmed [8] · Abdulgafar Kayode Amuda [3]

Abstract

The genesis and timing of molybdenum (Mo) mineralization in the Mada Ring Complex, north-central Nigeria, have been constrained using a combination of whole-rock elemental geochemistry, Nd-Sr isotopes, zircon U-Pb-Hf isotopes, and molybdenite Re-Os geochronological data. The Mada Ring Complex is one of fifty-three within-plate alkaline ring complexes with economically significant Sn and Nb production from largely alluvial placer deposits in north-central Nigeria. Molybdenum mineralization in the ring complex is dominantly disseminated with minor stockwork veins hosted within biotite granite. Integrated zircon U-Pb and molybdenite Re-Os geochronology constrain initial magma emplacement to between 152 and 151 ($\pm$ 1) Ma and the Mo-mineralization event to $\leq$ 150 ($\pm$ 1) Ma. The granites associated with Mo mineralization are highly silicic and display elevated whole-rock concentrations of Nb, Zr, Y, and REE (except Eu), as well as high $^{87}Rb/^{86}Sr$ ratios, but low concentrations of Sr, Ba, CaO, MgO, and TiO_2, consistent with highly differentiated A-type granites. They yield moderately negative whole-rock $\varepsilon Nd(t)$ (-5.87 to -5.47) and zircon $\varepsilon Hf(t)$ (-4.97 to -10.06), suggesting that their parental magmas were largely derived from the lower crust with a contribution from the upper mantle. Magmatic oxygen fugacity (fO_2) of the A-type granites (log FMQ = +1.16), constrained from zircon compositions, is lower than values reported from typical within-plate porphyry molybdenum deposits (log FMQ = +2 to + 3). However, compared to regional Sn $\pm$ Nb-mineralized A-type granites, the Mada A-type granites have higher fO_2 and Ce^{4+}/Ce^{3+}, but are less differentiated.

Keywords Magmatic differentiation · Crustal assimilation · Within-plate · A-type granite · Molybdenum · Jurassic

---

Editorial handling: P. Hollings

✉ Huan Li
lihuan@csu.edu.cn

1 Faculty of Earth Resources, State Key Laboratory of Geological Processes and Mineral Resources, China University of Geosciences, Wuhan 430074, China

2 Key Laboratory of Metallogenic Prediction of Nonferrous Metals and Geological Environment Monitoring, Ministry of Education, School of Geosciences and Info-Physics, Central South University, Changsha 410083, China

3 Department of Geology, Bayero University Kano, Kano, Kano State, Nigeria

4 State Key Laboratory of Biogeology and Environment Geology, School of Earth Sciences, China University of Geosciences, Wuhan 430074, China

5 Department of Geology, University of Cincinnati, Cincinnati, OH 42221-0013, USA

6 Department of Geology, Ahmadu Bello University Zaria, Zaria, Nigeria

7 Department of Geology, Gombe State University, P.M.B 127, Gombe, Gombe State, Nigeria

8 Department of Geology, Modibbo Adama University of Technology, Yola, Adamawa State, Nigeria

Introduction

Molybdenite, a major source of molybdenum (Mo) and rhenium (Re), is largely recovered from porphyry Mo and porphyry Cu (± Mo–Au) deposits, which collectively constitute > 50% of the global supply of these metals (Carten et al. 1993; Keith et al. 1993; Candela and Piccoli 2005; Cooke et al. 2020). Porphyry-related Mo ± Cu deposits have been broadly classified into three types (Carten et al. 1993; Sun et al. 2015; Audétat and Li 2017). The Dabie-type refers to collision-related molybdenum deposits that are largely confined to China, the largest global supplier of Mo (Mao et al. 2014; Sun et al. 2015; Ouyang et al. 2020). The Endako-type are large-tonnage, low-grade Cu ± Mo deposits associated with arc-related settings where Mo is recovered as a byproduct of Cu ores (Audétat and Li 2017). The Climax-type are low-tonnage, high-grade Mo deposits associated with highly fractionated within-plate silicic rocks (Carten et al. 1993). Largely based on their contrasting geochemical features, Carten et al. (1993) further subdivided the Climax-type into an alkalic subtype (e.g., Henderson, CO, USA) and a transitional subtype (e.g., Questa, NM, USA). Skarn-related Mo-Cu-W-Sn and greisen-related W-Mo-Bi-Sn deposits can also yield Mo in economic quantities (Černý et al., 2005; Kirwin 2012; Jiang et al. 2019).

In recent years, numerous studies based on whole-rock geochemistry, fluid and melt inclusions, and zircon U-Pb and molybdenite Re-Os systematics have significantly advanced our understanding of the genesis of molybdenum deposits, including their tectonic settings and age relationships with associated intermediate and silicic rocks (Lowenstern and Sinclair 1996; Klemm et al. 2008; Pettke et al. 2010; Mao et al. 2014; Mercer et al. 2014; Sun et al. 2015; Audétat and Li 2017; Li et al. 2017; Gaynor et al. 2019;; Ouyang et al. 2020). However, issues regarding the source(s) of Mo and the associated ore components (sulfur), especially in within-plate settings, have not yet been widely studied (Stein and Hannah 1985; Pettke et al. 2010; Mercer et al. 2014; Liu et al. 2019). For instance, given that world-class deposits are confined to a few regions, such as the western USA and the Dabie region of China, Pettke et al. (2010) argued that anomalously large Mo concentrations in the upper mantle and/or lower crust are necessary for formation of giant Mo deposits. Other studies suggest that several factors, such as the volume and redox conditions of mineralizing magmas, as well as the efficiency of metal extraction during late-stage magmatic-hydrothermal processes also play a crucial role in the formation of large Mo deposits (Mercer et al. 2014; Audétat and Li 2017; Ouyang et al. 2020). Consequently, understanding the origin of Mo deposits is therefore linked to determining the sources of metal and to deciphering factors that promoted its concentration in economically significant deposits (Mercer et al. 2014).

In this contribution, we present a combined study of whole-rock geochemistry, Nd-Sr isotopes, Re-Os geochronology, and zircon U-Th-Hf systematics of the Mada Ring Complex, one of the fifty-three Sn, Nb ± (Zn, Cu, Pb, Mo)-rich anorogenic alkaline complexes in north-central Nigeria collectively known as the Nigerian Younger Granite Province (NYG; Bowden et al. 1987; Girei et al. 2019a). Our primary objectives were to (i) determine the sources of magma and Mo, (ii) constrain the timing of magma emplacement and Mo mineralization, and (iii) compare the Mada Mo-mineralized granites with the associated Sn + Nb-mineralized granites in the Nigerian Younger Granite Province.

Regional geology

The Nigerian Younger Granite Province consists of 53 Mesozoic silica-oversaturated anorogenic syenite-granite ring complexes (Bowden et al. 1987; Girei et al. 2019a). The emplacement of these anorogenic ring complexes marked a period of extension that followed a prolonged hiatus (> 350 Ma) after the Neoproterozoic (600 ± 150 Ma) Pan-African Orogeny (Magaji et al. 2011; Martin et al. 2012). These anorogenic syenite-granite ring complexes cover a total area of 75,000 km^2 and form part of a larger alkaline province known as the Niger-Nigerian Alkaline Province (Fig. 1a–b; Kinnaird and Bowden 1987). This province, a classic example of within-plate alkaline magmatism, shows an age progression from Ordovician-Devonian (480–400 Ma) in Aïr (northern Niger) to Carboniferous (330–260 Ma) in Damagaram-Mounio (southern Niger) to Triassic-Early Cretaceous (213–141 Ma) in north-central Nigeria (Fig. 1b; Bowden et al. 1987). However, work by Moreau et al. (1994) demonstrated that the Aïr complex is structurally independent of the Damagaram-Mounio complex and the NYG. This necessitates the need for further geochronological studies to confirm the previously reported whole-rock Rr-Sr ages (Moreau et al. 1994; Ngako et al. 2006). In terms of petrological associations, peralkaline rocks and cogenetic anorthosite and leucogabbros predominate in Niger, whereas aluminous granites are dominant in Nigeria, where a few peralkaline granites occur in the northern alkaline ring complexes in association with syenite (Bowden et al. 1987; Demaiffe et al. 1991).

In Nigeria, 53 alkaline ring complexes have been identified, with diameters ranging from 2 to 25 km (Fig. 2a; Bowden 1985), each representing the root of an eroded volcano (Kinnaird et al. 1985). The complexes occur as high-level discordant intrusions in sets with overlapping centers (e.g., the Sara Fier, Ningi Bura, and Kila Wargi complexes) or as individual centers (e.g., the Ririwai, Mada, and Kudaru complexes; Fig. 2a). They are circular to elliptical in shape and intrude Precambrian basement consisting of high-grade
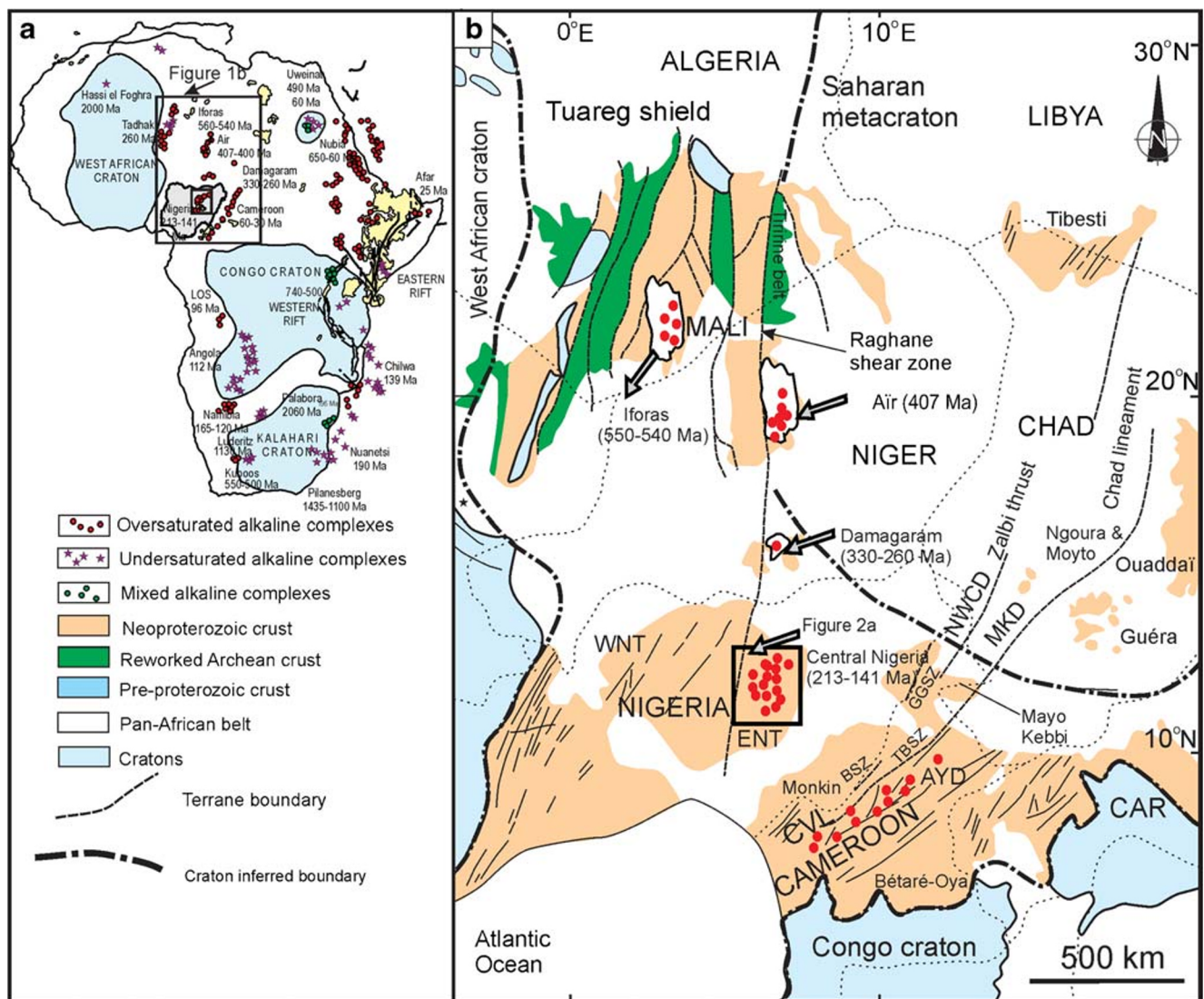
Fig. 1 (a) Sketch map showing the distribution of Phanerozoic anorogenic alkaline rocks in Africa (redrawn from Bowden et al. 1987); the black rectangle shows the location of b. (b) Sketch map showing the distribution of Phanerozoic anorogenic ring complexes in Iforas (Mali), Aïr (northern Niger), Damagaram-Mounio (southern Niger), north- central Nigeria, and Cameroon in relation to Pan-African continental structures of Western Gondwana (Aïr, northern Niger). The abbreviation CVL in (b) stands for Cameroon Volcanic Line; black rectangle in (a) shows the location of a

Eburnean (Paleoproterozoic) gneisses and migmatites with relics of Archean rocks, as well as Neoproterozoic (Pan-African) granites (Bowden et al. 1990; Bute et al. 2019; Girei et al. 2019b). The Neoproterozoic post-collisional granites in Nigeria are associated with Sn-Ta ± Nb-mineralized pegmatites that are largely confined to a NE-trending zone known as the Older Tin Belt (Girei et al. 2019a).

Emplacement of the alkaline ring complexes started in the Triassic (~ 213 Ma, e.g., Dutse Complex) and continued episodically until the Early Cretaceous (~ 141 Ma, e.g., Afu Complex), with a general progression from north to south (Fig. 2a; Rahaman et al. 1984; Girei et al. 2019a; Kamaunji et al. 2020). The distribution of alkaline ring centers along N-S shear zones and associated deep-seated transcurrent faults

indicate that zones of lithospheric weakness exerted significant control on their emplacement (Rahaman et al. 1984).

Primary Sn + Nb (±Zn, Cu, Pb) mineralization occurs in some of the Nigerian ring complexes, including the Ririwai, Tibchi, Afu, Ropp, and Ningi-Bura complexes, as well as in the Rayfield Gona pluton of the Jos-Bukuru Complex (Fig. 2a; Pastor and Turaki 1985; Kinnaird et al. 2016). Weathering and erosion of these epizonal alkaline complexes gave rise to economically significant alluvial Sn-Nb placer deposits that are mostly in proximity to the ring complexes (Girei et al. 2019a). Until this study, Mo mineralization has not been reported in the Mada Complex, but limited Mo mineralization associated with peralkaline granite has been reported from the Kigom Complex (Imeokparia 1985). Both Sn ± (Nb)- and
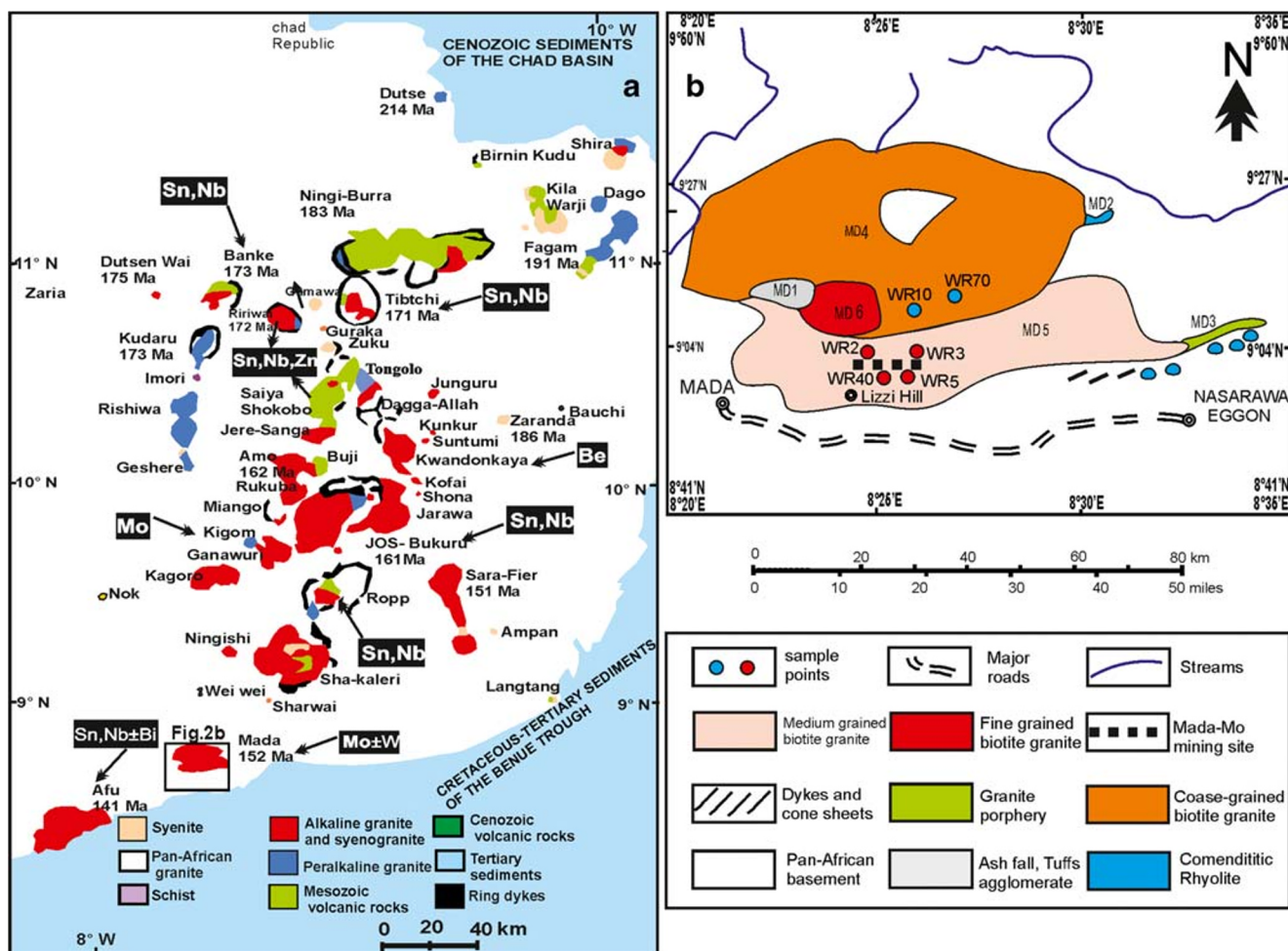
Fig. 2 (b) Simplified geological map showing the distribution of anorogenic ring complexes in north-central Nigeria (modified from Kinnaird et al. 1985). Note: the black rectangle in (a) shows the location of b. (b) Geological map of the Mada anorogenic ring complex (modified from Abaa 1985)

Mo-mineralized granites are spatially associated in the alkaline anorogenic province (Fig. 2a).

Geology of Mada Complex molybdenum mineralization

The Mada Complex is oval in shape, with axes measuring 26.5 km and 15 km, and occupies a total area of 271 km^2. It is composed of minor remnants of an extrusive phase, a large core of biotite granite, small outer dykes of granite porphyry, and minor mafic rocks that occur as dykes and cone sheets. The extrusive phase consists largely of comenditic rhyolite with minor breccia, ashfall, and agglomerate (Fig. 2b; Abaa 1985).

Biotite granite is the dominant intrusive phase in the Mada Complex. Largely based on texture, three facies of biotite granite have been distinguished: coarse-grained, medium-grained, and fined-grained. Molybdenum mineralization is confined to the medium-grained biotite granite (hereafter

"mineralized granite"; Fig. 2b). The mineralized granite experienced extensive hydrothermal alteration that is spatially associated with Mo mineralization (Fig. 3a–f). In thin section, the main minerals in mineralized granite and coarse-grained granite are quartz (30–32%), alkali feldspar (45–50%), plagioclase (10–13%), and biotite (4–6%), with zircon, apatite, and titanite as accessory minerals (Fig. 4a–i). The feldspar and quartz crystallized first, followed by biotite. Orthoclase constitutes the bulk of the alkali feldspar, and in mineralized granite, it is locally altered to sericite. Quartz grains are typically anhedral and relatively free of inclusions (Fig. 4b). Biotite occurs mainly as an interstitial mineral and ranges in color from light brown to green.

Molybdenum mineralization occurs in one of the southernmost anorogenic rings of the Mada Complex (Fig. 2a). Molybdenite constitutes the dominant ore mineral in the ring complex and occurs mainly disseminated in the cupolas of the mineralized granite, where it is associated with traces of wolframite (Fig. 3b–f). Two Mo ore-forming stages, each characterized by a distinctive mineral assemblage, have been

Fig. 3 **a** Coarse-grained biotite granite with barren quartz vein. **b–c** Alteration zones of Mada Mo mineralization (Stage I). **d** Contact between the Stage I and Stage II alteration zones. **e, f** Alteration zones of Mada Mo mineralization (Stage II)
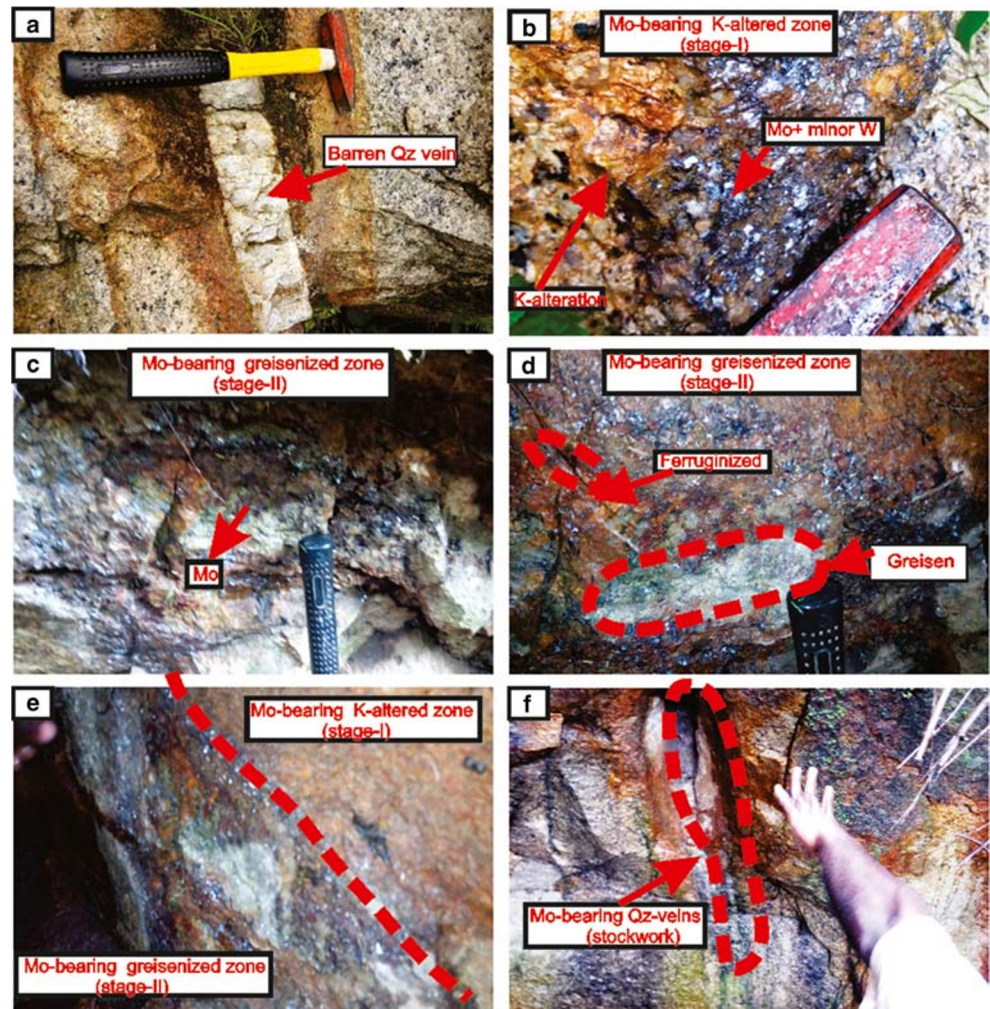
distinguished (Fig. 3b–d). During the first stage (Stage I, Fig. 3b), Mo mineralization was accompanied by hydrothermal alteration involving K-rich fluids. The alteration mineral assemblage includes K-feldspar, quartz, and minor sericite (Fig. 4d). This was followed by emplacement of disseminated and minor stockwork Mo mineralization during the second stage (Stage II, Fig. 3c, d). The alteration mineral assemblages that characterize the latter stage include sericite, chlorite, quartz, greenish mica, and minor pyrite (Fig. 4e–i). This mineral assemblage is similar to those observed in greisen-related deposits (Černý et al., 2005), and we therefore consider Stage II to represent greisen-related mineralization.

Sampling and analytical techniques

Sample collection

A total of six samples were collected: WR-02, WR-03, WR-05, and WR-40 are Mo-bearing samples of the mineralized granite collected from mine shafts, and WR-10 and WR-70 are samples collected from outcrops. All samples were analyzed for whole-rock geochemical and Nd-Sr isotopic composition. In addition, four samples (WR-02, WR-03, WR-05, and WR-40) were analyzed for Re-Os geochronology, and zircons were extracted from two samples (WR-02 and WR-10) and analyzed for U-Pb geochronology and Lu-Hf isotope compositions.

Whole-rock major- and trace-element analyses

Samples for whole-rock major- and trace-element analyses were crushed using a corundum jaw crusher and pulverized to 200 mesh size using an agate ball mill prior to analysis. Major-element analysis was performed using an energy-dispersive X-ray fluorescence (XRF) spectrometer (Shimadzu EDX 700), and trace-element analysis was performed using an Agilent 7700e inductively coupled plasma-mass spectrometer (ICPMS) with an analytical precision of ~ 5–10%. These analyses were carried out at the Australian Laboratory Services in Guangzhou, China. For XRF analysis, a pressed-powder disc was used following the procedure
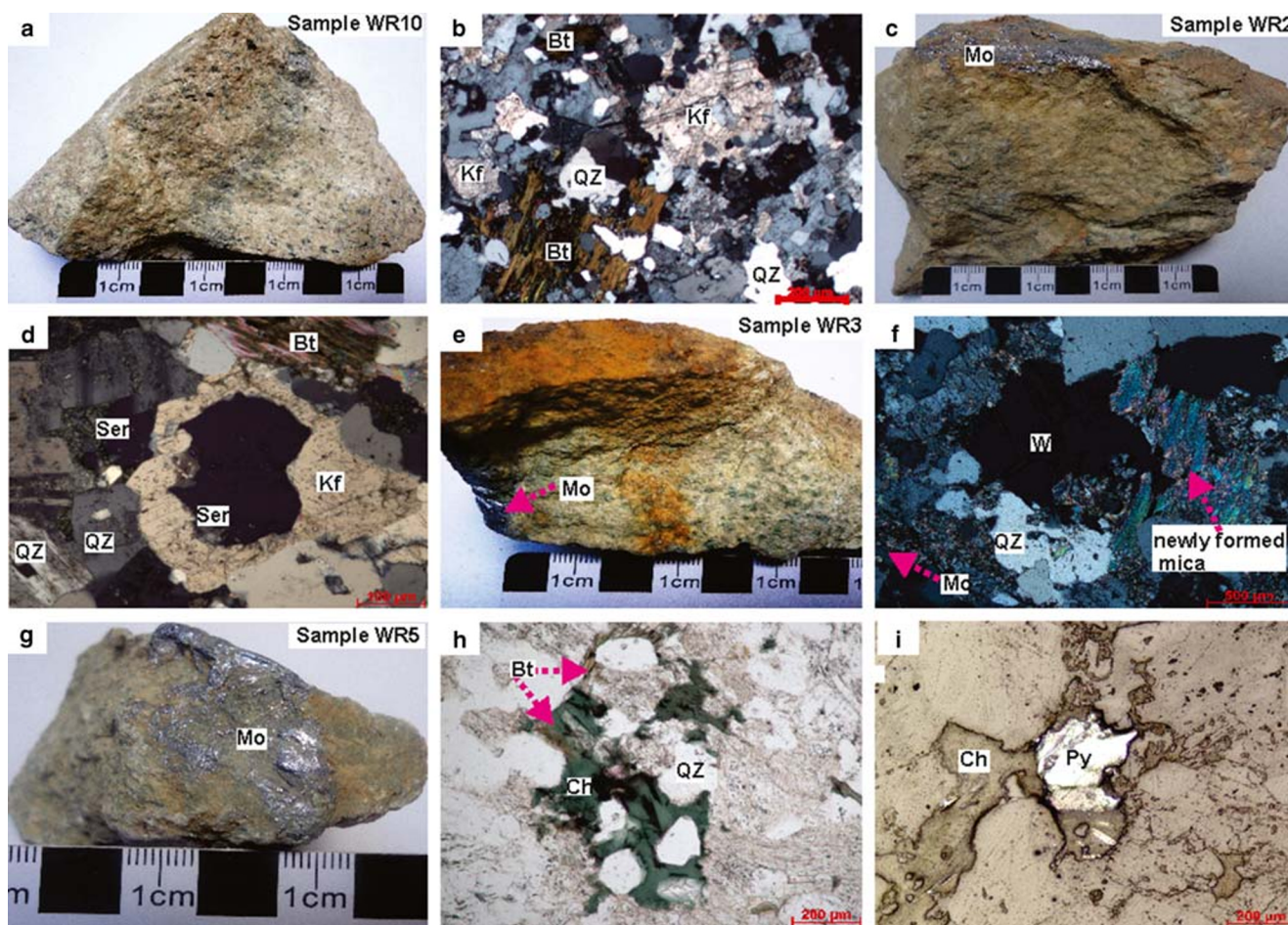
Fig. 4 **a–b** Coarse-grained biotite granite. **c–d** Medium-grained/mineralized biotite granite (samples from Stage I alteration zone). **e–f** Medium-grained/mineralized biotite granite (samples from Stage II alteration zone). Qz = quartz, Bt = biotite, Kf = K-feldspar, Ch = chlorite, Ser = sericite, Py = pyrite; Mo = molybdenite, W = wolframite

described in Girei et al. (2019a). Prior to the ICP-MS analysis, samples were dissolved sequentially with lithium borate fusion (by $Li_2B_4O_7$ flux) followed by aqua regia (HNO_3 + $3HCl$) digestion. International standard (JG-2) was used as a reference material for both major and trace elements.

Whole-rock Nd-Sr isotopes

Whole-rock Rb-Sr and Sm-Nd isotope analysis was performed on a Micromass Isoprobe Multi-Collector Inductively Coupled Plasma Mass Spectrometer (MC-ICP-MS) at the State Key Laboratory of Geological Processes and Mineral Resources (GPMR). Prior to the analysis, Sr and Nd were separated and purified using conventional ion exchange procedures. The procedure involved digesting ~ 50–100 mg of powdered sample into a distilled HF-HNO$_3$ solution in screw-top PFA beakers at a minimum temperature of 120 °C for 2 weeks. Rubidium and Sr were separated and purified using conventional column chemistry with cation exchange resins. Neodymium was separated from the other REEs using a di-(2-ethylhexyl) phosphoric acid (HDEHP)

column and purified with dilute HCl. During the analytical session, samples were analyzed alternately with the NBS-987 ($^{87}Sr/^{86}Sr = 0.710275 \pm 0.000012$; 2σ and $n = 11$) and JNdi-1 standards ($^{143}Nd/^{144}Nd = 0.512109 \pm 12$; 2σ) for Sr and Nd, respectively. The measured $^{87}Sr/^{86}Sr$ and $^{143}Nd/^{144}Nd$ values were corrected to $^{86}Sr/^{88}Sr = 0.1194$ and $^{146}Nd/^{144}Nd = 0.7219$, respectively (cf. Li et al. 2019). A single-stage neodymium model age was calculated assuming linear neodymium isotopic growth from a depleted mantle reservoir with εNd = 0 at $t = 4.56$ Ga to εNd = +10 at present, and a two-stage model age was calculated assuming that the protoliths of the granitic magmas had a $f_{Sm/Nd}$ value or Sm/Nd ratio equal to that of average continental crust (e.g., Jahn et al. 2001; Girei et al. 2019a).

Zircon U-Pb dating and Lu-Hf isotope analysis

Zircons for U-Pb dating and Lu-Hf isotope analysis were separated using conventional heavy liquid and magnetic separation techniques and then handpicked under a binocular microscope. The zircons were then mounted in epoxy resin and

polished prior to the LA-ICP-MS U-Pb dating and Lu-Hf isotope analysis. Cathodoluminescence (CL) images of the zircon grains were captured using a scanning electron microscope (SEM) fitted with an energy-dispersive system (EDS). U-Pb dating was performed on an Analytik Jena PQMS Elite ICP-MS coupled with an ESI NWR 193-nm laser ablation system at a 50-Hz frequency on a 32-μm ablation spot and a background acquisition time of 15 s (gas blank). The analysis was conducted at GPMR, China University of Geosciences (Wuhan), using zircon 91500 and glass NIST610 as external standards. Detailed analytical conditions including raw data selection, background integration, and time-drift correction are described by Liu et al. (2010). The analytical results for all standards used in zircon U/Pb dating are given in Electronic Supplementary Material (ESM) 1. Overall, the analyses yielded mean $^{206}Pb/^{238}U$ ages of 1063 ± 20 Ma (95% conf., MSWD = 1.4) for 91500, 600.3 ± 3.7 Ma (95% conf., MSWD = 0.3) for GJ-1, and 335.6 ± 8.4 Ma (95% conf., MSWD = 2.4) for PLE, which are all consistent with recommended values within error (Jackson et al. 2004; Slama et al. 2008).

Zircon Lu-Hf isotope analysis was carried out on ablation spots close to those previously analyzed for U-Pb ages. The analysis was performed at the GPMR on a Neptune Plus MC-ICP-MS coupled with a Geolas 2005 Excimer ArF laser ablation system with energy density of 5.3 J/cm^2. The procedure involves background signal acquisition for 20–50 s on laser mode with a beam diameter of 44-μm using zircon 91500 as a standard. Detailed procedures for correction of isobaric interferences of ^{175}Lu on ^{176}Hf and ^{176}Yb on ^{176}Hf are given in Machado and Simonetti (2001). Epsilon hafnium (εHf(t)) calculations were performed using the recommended present-day chondritic ratios of $^{176}Hf/^{177}Hf$ (0.282772) and $^{176}Lu/^{177}Hf$ (0.0332; Belousova et al. 2006).

Re-Os dating

Four molybdenum-bearing samples were selected for Re-Os isotopic dating: one sample (WR2) representing Mo mineralization associated with potassic alteration and three samples (WR3, WR4, and WR40) representing greisen-related Mo mineralization. Molybdenite grains were separated from the samples using gravity and magnetic techniques and then handpicked under a binocular microscope. The molybdenite Re–Os dating was performed at the State Key Laboratory of Isotope Geochemistry, Guangzhou Institute of Geochemistry, Chinese Academy of Sciences. Prior to analysis, chemical separation of Re-Os was performed using the Carius tube digestion technique. The procedure involved digesting 0.05 to 0.10 g of powdered sample and equilibrating it with ^{185}Re- and ^{190}Os-enriched spikes in reverse aqua regia (6 ml concentrated HNO_3 + 2 ml concentrated HCl) in sealed Carius tubes for 24 h at 240 °C. The Os fraction was extracted using a CCl$_4$ solvent and concentrated using hydrogen bromide (HBr) followed by microdistillation. In contrast, the Re fraction was separated and purified using anion column chromatography. The extracted osmium was loaded onto Pt filaments and measured as OsO_3^- ions by negative-thermal ionization mass spectrometry (N-TIMS) using the electron multiplier mode on a Thermo-Finnigan Triton. Repeated analyses of the Os standard solution yielded a mean $^{187}Os/^{188}Os$ value of 0.12048 ± 0.00028 (2 SD, $n = 5$), which is in good agreement with the value of 0.12022 ± 0.00020 (2 SD, $n = 14$) obtained on the same instrument in Faraday cup mode (Li et al. 2010). A Thermo Elemental X2 Series inductively coupled plasma mass spectrometer (ICP-MS) fitted with a conventional low-volume quartz impact bead spray chamber and a 0.4-ml min^{-1} borosilicate nebulizer was used to analyze the Re isotope ratio. In order to obtain high instrumental sensitivity and low oxide production levels, ion lens' settings and nebulizer gas flow rate and torch position were optimized daily using a 10-ng ml^{-1} tuning In–Ce mixture standard solution. The free aspiration of the nebulizer provided better signal stability. All data were blank corrected, and the total procedural blanks were 0.80 ± 0.40 pg (1σ, $n = 2$) with an $^{187}Os/^{188}Os$ ratio of 0.68 ± 0.54 (1σ, $n = 2$) on average for Os and 4.8 ± 0.2 pg (1σ, $n = 2$) for Re.

Results

Whole-rock major- and trace-element compositions

The whole-rock major- and trace-element compositions of the study samples are given in EMS 2 Table S1. The rocks have high SiO$_2$ (74.8 to 76.8 wt%) and K$_2$O (4.7 to 5.9 wt%), but low MgO (0.02 to 0.08 wt%), CaO (0.5 to 0.8 wt%), and TiO$_2$ (0.04 to 0.1 wt%), and moderate Na$_2$O + K$_2$O (7.7 to 8.1 wt%) and Al$_2$O$_3$ (11.7 to 12.4 wt%) concentrations. Compared to the coarse-grained biotite granite, the mineralized medium-grained granites have higher Na$_2$O but lower Al$_2$O$_3$ contents (EMS 2 Table S1). All granites have a metaluminous to weakly peraluminous composition (molar Al$_2$O$_3$/(Na$_2$O + K$_2$O > 1), similar to biotite granite associated with Sn ± Nb mineralization in the Ririwai and Tibchi complexes (Fig. 5a–d). However, granite associated with Mo mineralization in the Kigom Complex and rhyolite from the Mada Complex are peralkaline (Fig. 5c). All samples plot within the fields of (i) granite according to the classification of De la Roche et al. 1980; (Fig. 5a), (ii) high-K to shoshonitic granite in a K$_2$O vs. SiO$_2$ discrimination diagram, (iii) alkali calcic to calc-alkalic granite according to the classification of Frost et al. 2001; (Fig. 5b, d), and (iv) within-plate setting on the discrimination plot of Pearce et al. (1984), a characteristic feature of within-plate A-type granite (Bonin 2007; Fig. 5e–f). However, A-type granites associated with Sn ± Nb mineralization in the

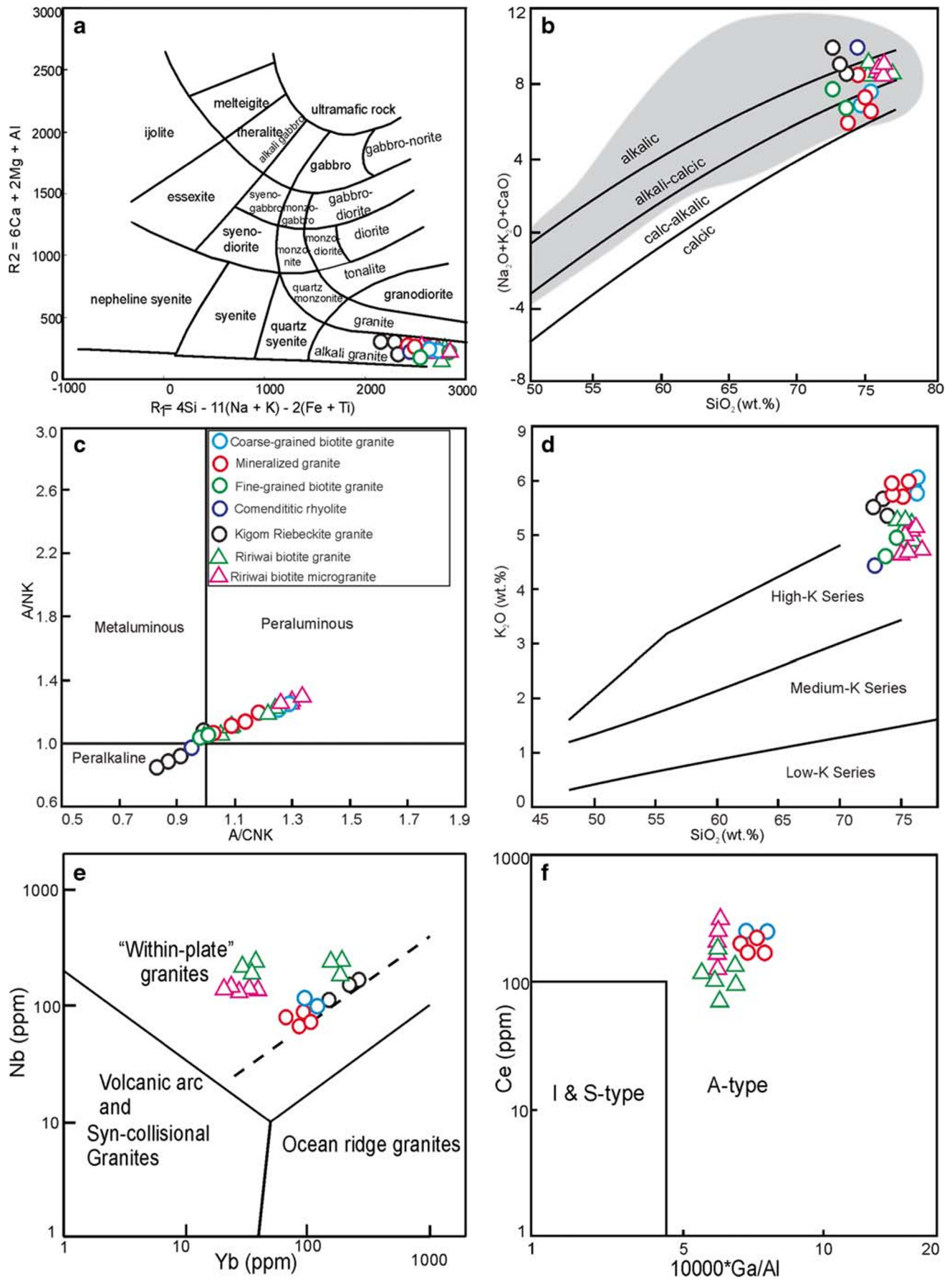◀ **Fig. 5** Granite classification diagrams. **a** SiO_2 versus $Na_2O + K_2O$ plot of Mada granite (after De la Roche et al. 1980). **b** SiO_2 versus ($Na_2O + K_2O - CaO$) plot of Mada granite, after Frost and Frost et al. (2001). **c** A/CNK versus A/NK plot of Mada granite, (after Shand 1943). **d** SiO_2 versus K_2O plot of Mada granite, (after Peccerillo and Taylor, 1976). **e** $10,000 \times$ Ga/Al versus Ce plot of Mada granite, after Whalen et al. (1987). **f** Yb versus Nb plot of Mada granite, after Pearce et al. (1984). Data of granites plotted for comparisons are from Abaa (1985), Imeokparia (1985), Batchelor and Bowden (1986), and Girei et al. (2019a, b)

Ririwai and Tibchi complexes generally have higher SiO_2 and lower K_2O than those associated with Mo in the Mada and Kigom complexes (Fig. 5d).

All samples are characterized by slight enrichment of LREEs relative to HREEs along with a negative Eu anomaly (Fig. 6a–b). On a primitive mantle-normalized plot (Fig. 6a), the samples show trace-element patterns characterized by large enrichments of Zr, Hf, and Rb and depletions of Sr, Ba, and P, consistent with a magma evolution marked by significant fractionation of feldspars and apatite. Samples of the coarse-grained granite generally have higher Nb, Ta, La, Zr, Rb, and Ba than the mineralized granite (EMS 2 Table S1). Calculated zircon saturation thermometry based on the model of Watson and Harrison (1983) yielded temperature estimates ranging from 838.0 to 860.0 °C (EMS 2 Table S1).

Whole-rock Sr-Nd isotopes

Whole-rock Sr-Nd isotope compositions are given in Table 1. Initial ($^{87}Sr/^{86}Sr$) and $\varepsilon Nd(t)$ were calculated using the zircon U-Pb ages of the granites. The samples yielded high $^{87}Rb/^{86}Sr$ values ranging from 62.0 to 78.7, but low ($^{87}Sr/^{86}Sr$)$_i$ values ranging from 0.6949 to 0.7044, with one value (0.6949) falling below the basaltic achondrite best initial (BABI = 0.69897 ± 3; Villaseca et al. 1998). Such anomalously low initial $^{87}Sr/^{86}Sr$ values indicate the Rb-Sr system was probably

disturbed (Ahmed et al. 2018). The $^{143}Nd/^{144}Nd$ values range from 0.5122 to 0.5123 and calculated $\varepsilon Nd(t)$ from -5.87 to -5.47, corresponding to Mesoproterozoic two-stage models ages ranging from 1243 to 1587 Ma. Calculated $\varepsilon Nd(t)$ values of the Mada molybdenum-related biotite granite are slightly higher than the $\varepsilon Nd(t)$ values (-3.55 to -3.26) of the Sn-rich biotite granite from the Ririwai Ring Complex in north-central Nigeria (Girei et al. 2019a).

Zircon U-Pb geochronology

Analytical results of zircon U-Pb dating are given in EMS 2 Table S2. The zircon grains are generally large (100–200-μm diam.), euhedral to prismatic in shape, and pale yellow to gray in color. They exhibit concentric oscillatory zoning and display (100) and (101) crystallographic form (ESM 3 Fig. 1). Zircon grains from the coarse-grained biotite granite ($n = 14$) exhibit Th/U ratios ranging from 0.88 to 1.40, which are typical of magmatic zircon (Belousova et al. 2002; Kirkland et al. 2015). Eight zircon grains yielded $^{206}Pb/^{238}U$ ages ranging from 152 to 155 Ma, with a weighted mean age of 152.6 ± 1.1 Ma (MSWD = 0.34) (Fig. 7a–b), which is similar to a whole-rock Rb-Sr age of 147 ± 5 Ma (initial strontium = 0.708 ± 0.02) from Rahaman et al. (1984). In addition, four zircon grains yielded younger $^{206}Pb/^{238}U$ ages ranging from 148 to 149 Ma, suggesting a degree of Pb loss.

Thirty spots were dated on the zircon grains extracted from the mineralized granite, but eight spots were rejected due to high common Pb and/or low concordance (< 90%). The remaining 22 zircon grains yielded magmatic Th/U ratios ranging from 0.82 to 1.55 and formed two age clusters. The older one consists of eight $^{206}Pb/^{238}U$ ages, ranging from 159.0 to 163.0 Ma with a weighted mean age of 160.0 ± 1.1 Ma (MSWD = 1.03), that are interpreted as antecrystic zircon grains that crystallized from an earlier pulse of magma
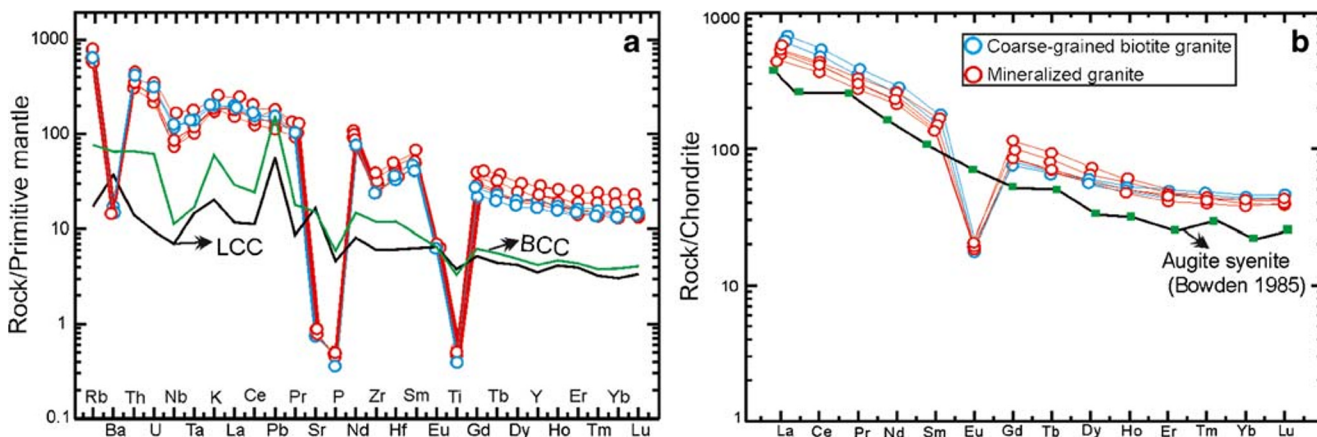

Fig. 6 **a** Chondrite-normalized REE plot of Mada granite, with normalization values from Taylor and McLennan (1985). **b** Primitive-mantle-normalized trace element spider diagrams of Mada granite, with normalization values from Sun and McDonough (1989). Note: green and black lines in (**a**) represent average composition of bulk continental crust (BCC) and lower continental crust (LCC) as reported by Taylor and McLennan (1985). Black and green line in (**b**) represent REE pattern of Augite syenite from Kila Warji Complex (Bowden 1985)

Table 1 Whole-rock Nd-Sr Isotope compositions of the Mada granites

Sample no.	WR10	WR70	WR2	WR3	WR40	WR5
Rb (ppm)	438	438	390	394	375	386
Sr (ppm)	15.9	16.2	17.3	18.2	15.8	16.7
$^{87}Rb/^{86}Sr$	78.7	79.4	66.1	62.1	69.6	67.8
$^{87}Sr/^{86}Sr$	0.8732	0.8665	0.8432	0.8367	0.8523	0.8489
2σ	0.000007	0.000006	0.000007	0.000006	0.000006	0.00001
$(^{87}Sr/^{86}Sr)_i$	0.7031	0.6949	0.7023	0.7044	0.7038	0.7043
Sm (ppm)	19.2	19.2	21	26.3	20.2	20.4
Nd (ppm)	108	109.5	106.5	121.5	98.6	104.5
$^{147}Sm/^{144}Nd$	0.1072	0.1057	0.1192	0.1309	0.1239	0.118
$^{143}Nd/^{144}Nd$	0.51225	0.512269	0.512272	0.512286	0.512274	0.512267
$\pm 2\sigma$	0.000006	0.000005	0.000005	0.000004	0.000005	0.000005
fSm/Nd	− 0.46	− 0.46	− 0.4	− 0.34	− 0.37	− 0.4
εNd (t)	− 5.87	− 5.47	− 5.65	− 5.6	− 5.72	− 5.73
T_{DM1} (Ma)	1288	1243	1414	1587	1485	1404
T_{DM2} (Ma)	1243	1414	1587	1485	1404	1407

T_{DM1}, single-stage model age, computed by assuming a linear Nd isotopic growth involving a depleted mantle reservoir; T_{DM2}, two-stage model stage, computed by assuming that the fSm/Nd of granitic protolith equal to that of the average continental crust
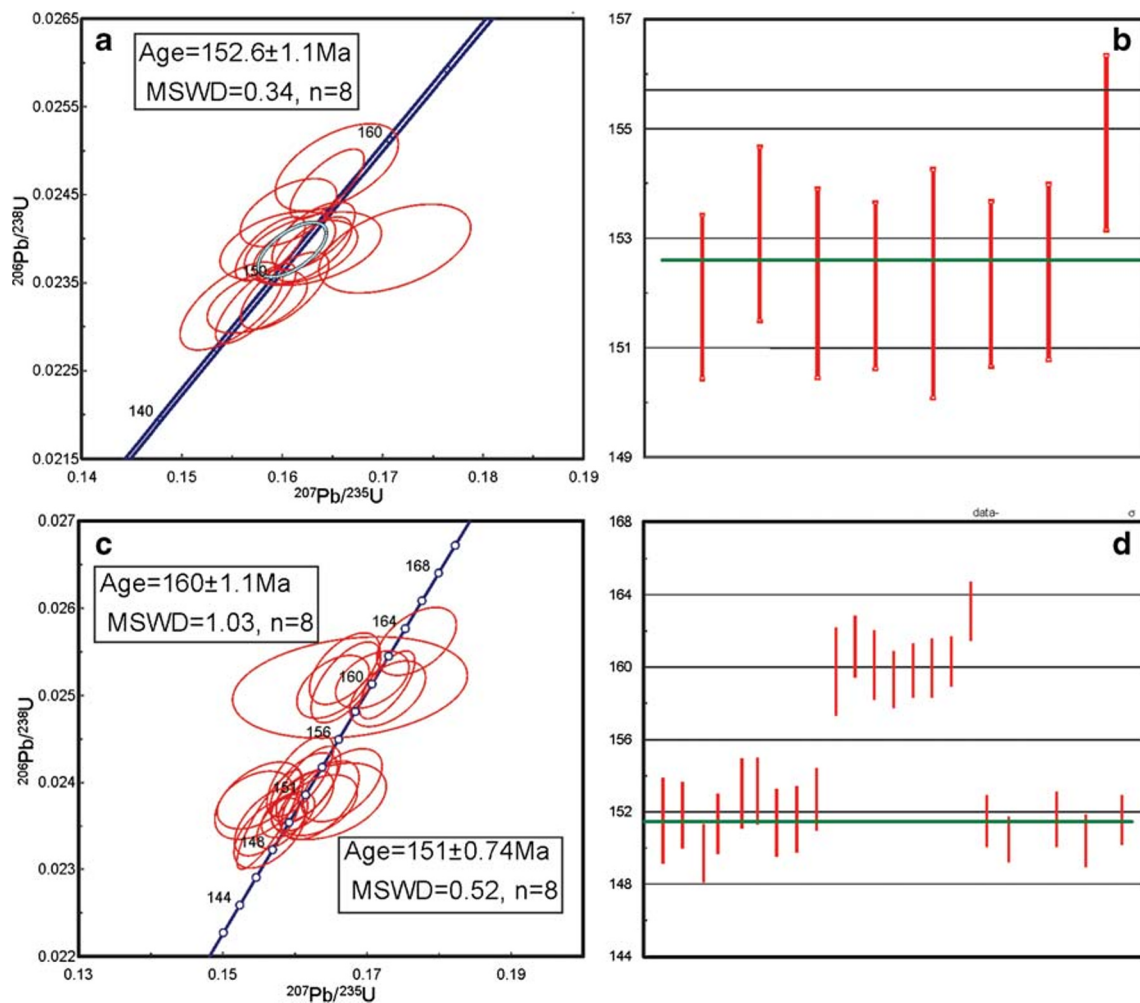

Fig. 7 a Zircon U-Pb age concordia plot for the coarse-grained biotite granite. **b** Mean weighted average age plot for coarse-grained biotite granite. **c** Zircon U-Pb age concordia plot for mineralized granite. **d** Mean weighted average age plot for the mineralized granite

(Miller et al. 2007). The younger population consists of fourteen $^{206}Pb/^{238}U$ ages, scattered between 149 and 153 Ma with a weighted mean age of 151 ± 0.74 Ma (MSWD = 0.52; Fig. 7c–d), that are interpreted to represent the crystallization age of the rock. Thus, the younger zircons are "autocrysts" that crystallized from their host melt near the time of emplacement (Miller et al. 2007).

Zircon trace-element compositions

The trace-element compositions of zircon from the Mada granite are given in EMS 2 (Table S3). The zircons yield moderate, but variable concentrations of U (143–2133 ppm) and Th (43–859 ppm), with fairly high Th/U ratios (0.88–1.55) that are typical of magmatic zircon (Kirkland et al. 2015). They are also characterized by high concentrations of Hf (8029–17,910 ppb), but low Nb/Ta ratios (0.57–4.18), reflecting growth from a highly fractionated melt. In addition, the zircons exhibit wide variations in elements, such as Y (1102–5491 ppm), Pb (8.7–134 ppm), Ti (3.5–15.1 ppm), and ∑REE (1010–3932 ppm). On a chondrite-normalized REE diagram, they exhibit steeply rising patterns characterized by HREE enrichment and LREE depletion, with a positive Ce anomaly and a negative Eu anomaly (ESM 3 Fig. 2a–c). However, a few zircons, especially those in the mineralized granite, have high LREE contents and low Sm_N/La_N ratios, which can be attributed to hydrothermal alteration and/or the presence of LREE-rich accessory minerals, such as apatite (ESM 3 Fig. 2d–e).

Zircon Hf isotopes

Analytical results of in situ zircon Hf isotopes are given in EMS 2 (Table S4). Five zircons of the coarse-grained biotite granite yielded $^{176}Hf/^{177}Hf$ ranging from 0.28243 to 0.2845 and $^{176}Yb/^{177}Hf$ from 0.0291 to 0.0576. Calculated εHf(t) values range from − 8.25 to − 9.85, corresponding to late Paleoproterozoic crustal model (T^C_{DM}) ages of 1723–1764 Ma (EMS 2, Table S4). Twelve spots were analyzed on ten zircons (including two antecrystic grains) of the mineralized granite; one of the antecrystic grains (Wr2–14) yielded the highest values of $^{176}Hf/^{177}Hf$ (0.2426),

$^{176}Yb/^{177}Hf$ (0.0985), and calculated εHf(t) (− 4.97), whereas the other antecrystic grain (Wr2–12) yielded values of $^{176}Hf/^{177}Hf$ (0.2824), $^{176}Yb/^{177}Hf$ (0.0521) and εHf(t) (− 8.77) that overlap the range obtained from the autocrystic grains ($^{176}Hf/^{177}Hf$ = 0.2424–0.2425, $^{176}Yb/^{177}Hf$ = 0.0339–0.0765, and εHf(t) = − 5.12 to − 10.06; EMS 2, Table S4). Calculated crustal model ages (T^C_{DM}) range from 1839 to 1526 Ma, with the lowest value (1526 Ma) obtained from the antecrystic grain that yielded the highest εHf(t) (EMS 2, Table S4). Overall, calculated crustal model ages are slightly lower than, but overlap the range of, two-stage model ages (1243 to 1587 Ma) obtained from whole-rock Nd isotopes (Table 1).

Molybdenite Re-Os geochronology

The analytical results of molybdenite Re–Os dating for four samples are given in Table 2. Because the common Os contents in the molybdenite are negligible, model ages were calculated using the equation {ln $(^{187}Os/^{187}Re + 1)/\lambda$} (Suzuki et al. 2001), where λ is the decay constant of ^{87}Re, which is equal to $1.666 (\pm 0.017) \times 10^{-11}$ year^{-1} (Smoliar et al. 1996). The molybdenite-bearing sample associated with potassic alteration (WR2) yielded Re (238 ppb), ^{187}O (260.6 pbb), and a calculated model age of 150.9 ± 1 Ma that, within error, agrees well with the zircon weighted mean $^{206}Pb/^{238}U$ age (151.3 ± 0.74 Ma) obtained from the same sample. This age (150.9 ± 1 Ma) is therefore interpreted as the approximate age of the Mo ore-forming event in the Mada Ring Complex. In contrast, the three molybdenite-bearing samples from greisen-related Mo mineralization (WR3, WR4, and WR40) exhibit wide variations of Re (95.9 to 269.0 ppb), ^{187}O (123.6 to 217.6), and calculated model ages (144 to 136.9 Ma; mean = 142 ± 11 Ma). For a given aliquot size (i.e., 0.1 g), the sample with the lowest Re content (95.9 ppb) yielded the youngest model age (136.9 Ma), and the mean model age obtained from these samples (142 ± 11 Ma) is significantly younger than their Re-Os isochron age (155.3 ± 7.2 Ma; MSWD = 0.23; initial $^{187}O/^{188}O$ = $− 6.6 \pm 9.8$; Fig. 8a, b). These ages cannot therefore be interpreted to represent ore formation age, but indicate that the Re-Os system was probably disturbed (Suzuki et al. 2001).

Table 2 Molybdenite Re-Os geochronological data of the Mada mineralized granite

Samples	Re (ppb) Measured	2σ	Common Os (ppb) Measured	2σ	^{187}Re (ppb) Measured	2σ	^{187}Os Measured	2σ	Model age (Ma)	2σ
WR2	238.0	3.5	0.3897	0.0043	103,528	1886	260.6	3.0	150.9	1.0
WR3	269.0	3.0	0.4234	0.0037	89,422	1268	215.7	1.8	144.6	1.0
WR5	225.3	2.0	0.3533	0.0028	90,615	1056	217.6	1.7	144.0	1.0
WR40	95.9	2.3	0.1469	0.0013	54,112	1399	123.6	0.9	136.9	1.0

Discussion

The geochemical data permit evaluation of magma sources and intrusive history related to molybdenum mineralization in the Mada Ring Complex of north-central Nigeria. Evaluation of these data and comparison with studies of Sn ± Nb mineralization in the NYG Province enables us to offer new insights into the petrogenetic factors that favor formation of co-existing Mo and Sn ± Nb Mineralization.

Timing of magma emplacement and Mo mineralization

Our combined LA-ICP-MS zircon U-Pb and molybdenite Re-Os geochronological data provide insights into the timing of magma emplacement in relation to the Mo mineralization event at Mada. A previous study of the Mada Complex yielded a whole-rock Rb-Sr age of 147.0 ± 5 Ma, interpreted to represent its emplacement age (Rahaman et al., 1985). However, as previously stated, the low initial $^{87}Sr/^{86}Sr$ values of Mada granite relative to their negative $\varepsilon Nd(t)$ values (Table 1) suggest that their Rb-Sr system was probably disturbed (Villaseca et al. 1998). Thus, the whole-rock Rb-Sr ages of the granite may be lower than its actual emplacement age (Walraven et al. 1990). Nevertheless, the age is within error of the weighted mean zircon $^{206}Pb/^{238}U$ age of 152.6 ± 1.1 Ma obtained for the coarse-grained biotite granite (Fig. 7a–b). On the other hand, zircons from the mineralized granite yielded $^{206}Pb/^{238}U$ ages ranging from 163 to 150 Ma, with two distinct clusters: (1) an older mean age of 160 ± 1 Ma ($n = 8$) and (2) a younger mean age of 151 ± 0.7 Ma ($n = 14$; Fig.

7c–d). The $\sim 160 \pm 1$ Ma age closely matches the $^{206}Pb/^{238}U$ age of the biotite granite from the nearby Ropp complex (161 ± 0.8 Ma; Vandi Dlama Kamaunji, pers. comm., 2020), implying that older zircons may be antecrystic (Miller et al. 2007; Gaynor et al. 2019). Thus, assuming Pb-loss can be discounted, the younger age (151 ± 0.7 Ma) represents the approximate crystallization age of the mineralized granite.

LA-ICP-MS molybdenite Re-Os dating yielded a wide range of model ages (136.9 to 150.9 Ma; Table 2). A single molybdenite-bearing sample associated with potassic alteration yielded a model age of 150.9 ± 1 Ma, coeval with the U/Pb age of the mineralized granite (151 ± 0.7 Ma), and is interpreted as the approximate age of commencement of Mo mineralization in the study area. In contrast, three molybdenite-bearing samples from greisen-related Mo mineralization yielded dissimilar model ages ranging from 144.0 to 136.9 Ma with a mean of 142.0 ± 11.0 Ma, which is younger than their isochron age (155.3 ± 7.2 Ma). When the Re-Os system remains closed, the mean model age of molybdenites will agree reasonably well with their Re-Os isochron age, and can be interpreted as the time of ore formation (Selby et al. 2003; Stein 2013; Zhai et al. 2019). However, given the stark disagreement between the mean model age and the isochron age, neither can be interpreted with assurance to represent the age of Stage II mineralization in the Mada Complex. Instead, such ages suggest that the Re-Os system was probably disturbed due to open-system processes (e.g., Re loss; Stein et al. 1998; Suzuki et al. 2001) or decoupling related to heterogeneous distribution of Re in molybdenite caused by variation in the physicochemical properties of the mineralizing fluids (Barra et al. 2017). Thus, the magma emplacement and Mo mineralization event in the Mada Ring Complex probably took place between 152 ± 1 and 150 ± 1 Ma.
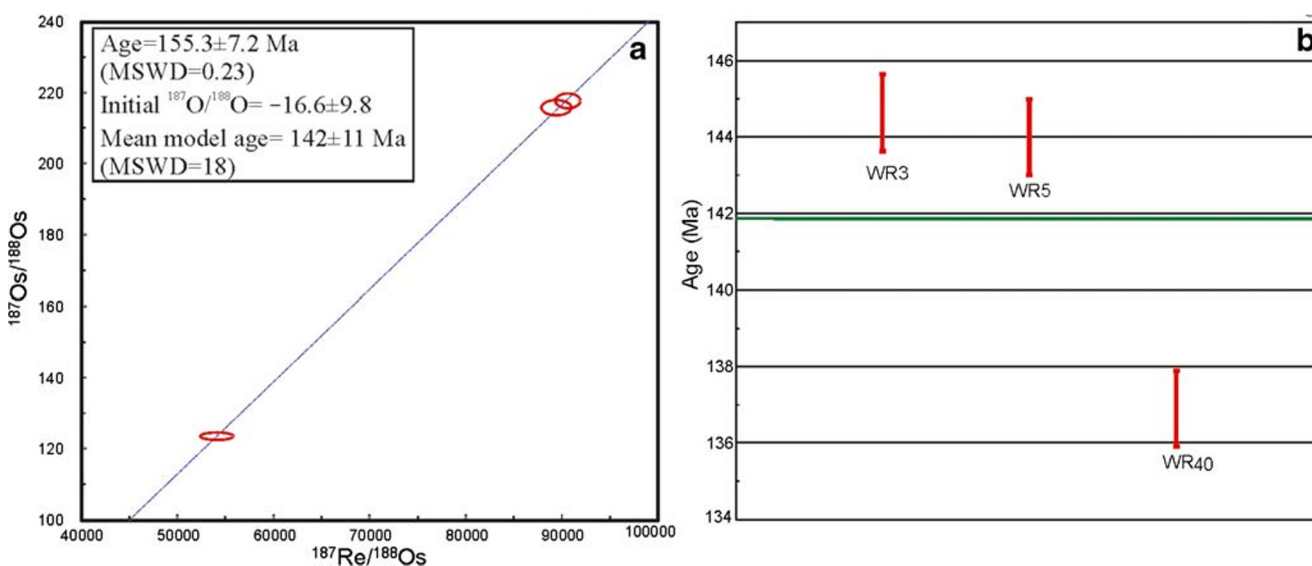

Fig. 8 **a** $^{187}O/^{188}O$ versus $^{187}Re/^{188}Os$ isochrone for the Mada molybdenite sample. **b** Plot showing distribution of calculated model ages of three molybdenite samples from greisen-related Mo mineralization

Source of magma and molybdenum

A-type granites associated with Mo mineralization in the Mada Ring Complex are highly silicic with low MgO, CaO, TiO_2, Sr, and Ba consistent with highly differentiated granite (Yakymchuk 2019). The high degree of fractionation means that their major- and trace-element compositions cannot provide reliable information regarding the possible source(s) of their parental magma(s) (Christiansen and Keith 1996; Girei et al. 2019a).

Paired Sm-Nd and Rb-Sr isotope analyses are widely regarded as a robust tool for constraining the source of a granite magma (Dickin et al. 1991; Li et al. 2018, 2018). However, in highly differentiated granites associated with mineralization, the Rb-Sr system may be disturbed as a result of open-system processes such as loss of radiogenic strontium (^{87}Sr), which usually gives rise to low initial Sr ratios ($^{87}Sr/^{86}Sr)_I$ (Walraven et al. 1990). The Mada A-type granites yield low ($^{87}Sr/^{86}Sr)_i$ (0.6949 to 0.70440), with one value (0.6949)

falling below BABI (0.69897 ± 3), suggesting that their Rb-Sr isotopic systems have been disturbed (Fig. 9a; Walraven et al. 1990; Li et al. 2019). As a result, the initial strontium ratio of such granites cannot be used to constrain their source (Ahmed et al. 2018). In contrast, the Sm-Nd system is more resistant to fluid-induced isotopic disturbance and can provide more reliable constraints on the parental source(s) of the mineralized granites (Jiang 2005; Li et al. 2018, 2018). Thus, assuming that equilibrium conditions existed between the melt and residual crystals during the partial melting event that led to generation of the Mada A-type magmas, the Nd isotope composition of the granites still reflects their sources the isochron age (Poitrasson et al. 1995; Christiansen and Keith 1996). The Mada granites yield $\epsilon Nd(t)$ values (-5.87 to -5.47) lower than those of Sn $\pm$ Nb-mineralized granite in the Ririwai complex (-3.55 to -3.26) but higher than those of the Pan-African basement in the region (-8.4 to -20.9; Fig. 9b; Girei et al. 2019a, b), suggesting magma derivation involving large amounts of crustal material with time-integrated Nd
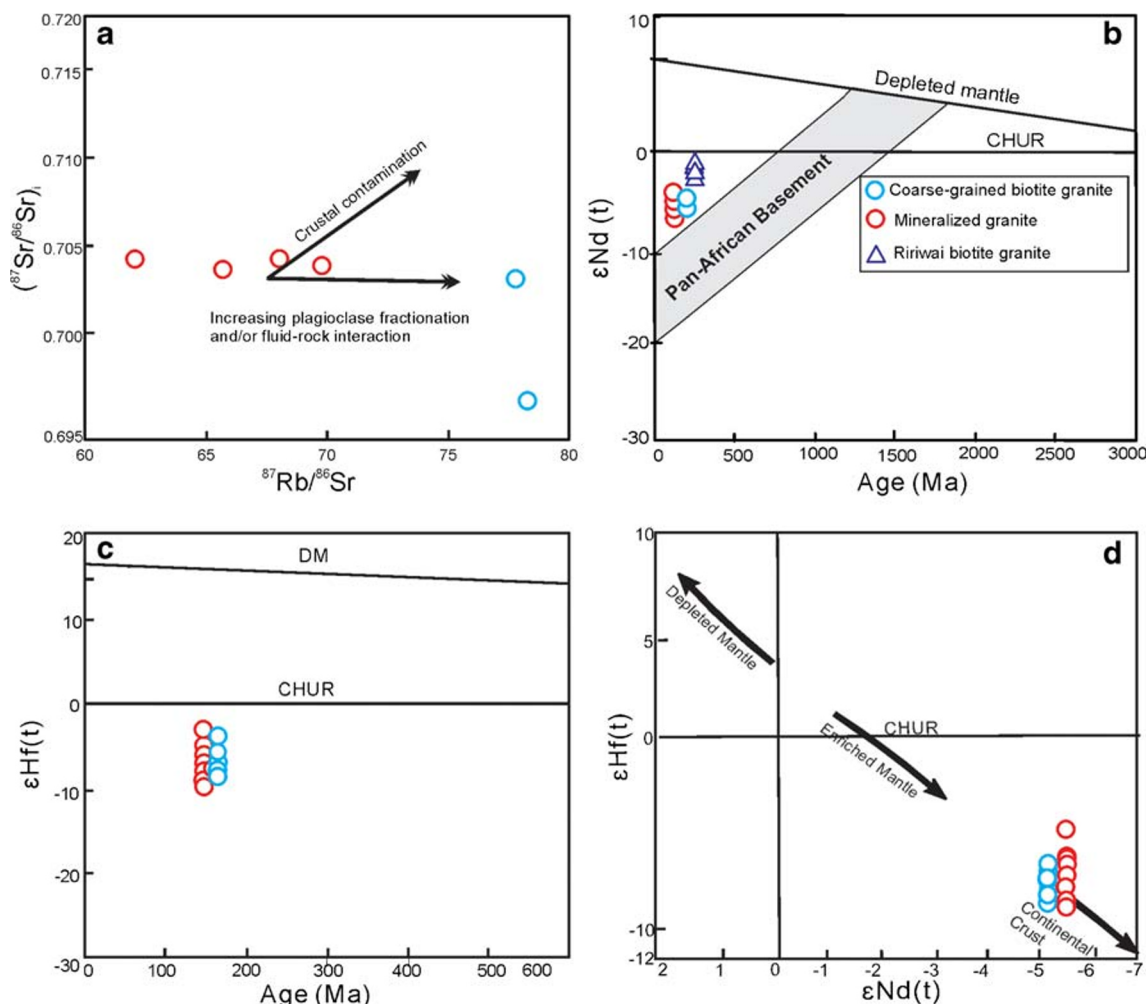

Fig. 9 **a** Whole-rock ($Sr^{87}/Sr^{86})_i$ vesus Rb^{87}/Sr^{86}. **b** Plot of whole-rock $\epsilon Nd(t)$ versus age for Mada granite. **c** Plot of zircon $\epsilon Hf(t)$ versus age for Mada granite. **d** Zircon $\epsilon Hf(t)$ versus whole-rock $\epsilon Nd(t)$ isotopic plots for

the Mada granites. Whole-rock $\epsilon Nd(t)$ data of Ririwaai Sn $\pm$ Nb-mineralized granite are from Girei et al. (2019a, b)

enrichment relative to the chondrite uniform reservoir (CHUR), along with a moderate contribution from the upper mantle (Fig. 9b; e.g., Dickin et al. 1991; Kerr and Fryer 1993). This is consistent with the zircon Lu-Hf results, which exhibit moderate negative yet variable εHf(t) values (Fig. 9c–d).

A growing body of literature has shown that the rhenium (Re) content of molybdenite can provide insight into possible sources of the ore metals (Mao et al. 1999; Stein et al. 2001; Berzina et al. 2005; Mao et al. 2006; Stein 2006; Wanhainen et al. 2014). In this regard, high Re contents (> 100 ppm) in molybdenite suggest a mantle source for Mo, whereas low Re contents (< 10 ppm) are consistent with a crustal source (Mao et al. 1999; Berzina et al. 2005). Although molybdenite at Mada generally has low Re contents (< 1 ppm; Table 2), favoring a crustal source for the metal, it should be noted that the Re content of molybdenite is also a function of the redox conditions of the melt from which it crystallizes, as highly oxidizing melts are known to partition large amounts of Re into molybdenite (Berzina et al. 2013; Barton 2019). Thus, molybdenite associated with porphyry Cu ± Mo deposits, which usually forms from highly oxidizing magmas, generally has higher Re contents relative to those that form from less oxidizing magmas (Barton 2019). In this regard, until further evidence becomes available, the possibility of mantle contribution to the ore materials (Mo and S) of the Mada Mo mineralization cannot be completely ruled out.

Zircon constraints on temperature and redox conditions

Various elements substitute readily into the zircon structure, providing information about the physicochemical conditions of its growth (Ferry and Watson 2007; Claiborne et al. 2010; Trail et al. 2012; Smythe and Brenan 2016). In particular, Ti-in-zircon thermometry can provide reliable constraints on magma temperature at the time of zircon crystallization (Ferry and Watson 2007; Siégel et al. 2018; Schiller and Finger 2019). However, given that Ti is preferentially incorporated into rutile and can substitute for Si in the zircon structure, Ti-in-zircon temperatures are partly dependent on the activity of silica (a_{SiO_2}) and titanium oxides (a_{TiO_2}) in the melt (Ferry and Watson 2007). Given that the Mada granites are highly silicic and contain no rutile, we adopted activity values of 1.0 and 0.7 for silica and titanium oxides, respectively (e.g., Li et al. 2014). For the Mada granites, calculated temperatures using the modified thermometric equation of Ferry and Watson (2007) range from 705 to 794 °C, which are slightly lower than temperature estimates based on the Zr-saturation thermometry model (838 to 860 °C; Watson and Harrison, 1983; EMS 2, Table S5). This difference may reflect the presence of antecrystic zircons in the Mada granite, leading to overestimation of zircon saturation temperatures computed using the model of Watson and Harrison (1983), as noted

for A-type granites from the Ririwai Complex in north-central Nigeria (Girei et al. 2019a).

Numerous studies have demonstrated that magmatic redox conditions significantly affect partitioning of REEs, especially Eu and Ce, into zircon structure (Ballard et al. 2002; Trail et al. 2012; Burnham et al. 2015; Smythe and Brenan 2016). Unlike other REEs which are exclusively trivalent, Eu and Ce can undergo changes in valence, i.e., between (II) and (III) for Eu and between (III) and (IV) for Ce, depending on the redox conditions of the melt (Trail et al. 2012). Under oxidizing conditions, the tetravalent form of Ce (Ce^{4+}) has a similar radius and the same charge as Zr^{4+} and hence is more compatible in the zircon structure than Ce^{3+}. Under the same (oxidizing) conditions, Eu occurs as Eu^{3+}, which can be readily accommodated in the zircon structure giving rise to a small (less negative) Eu anomaly (Ballard et al. 2002; Wu et al. 2018). High Ce^{4+}/Ce^{3+} and low Eu/Eu* in zircon therefore indicate oxidizing conditions at the time of crystallization (Ballard et al. 2002). However, Eu/Eu* in zircon is sensitive to melt Eu/Eu∗, which is chiefly controlled by plagioclase fractionation and/or accumulation (Burnham et al. 2015). Thus, given the presence of plagioclase in the Mada granite, Eu/Eu* cannot provide a reliable estimate of oxygen fugacity (Smythe and Brenan 2016). Zircons from the Mada granite yield moderate, yet variable, Ce^{4+}/Ce^{3+} values with higher Ce^{4+}/Ce^{3+} in the mineralized granite than in the coarse-grained biotite granite, indicating intermediate magmatic redox conditions at the time of zircon crystallization (Fig. 10a–b; EMS 2, Table S5). Moreover, calculated oxygen fugacity using the lattice strain model (Smythe and Brenan 2016) all plot above the field of the fayalite-magnetite-quartz (FMQ) buffer on a $-\log fO_2$ vs T/°C diagram, with higher average oxygen fugacity values (log FMQ = +1.16; Fig. 10a) in the mineralized granite than in the coarse-grained biotite granite (log FMQ = +0.45). Thus, it can be inferred that the A-type granite magmas associated with Mo mineralization in the Mada Complex were moderately oxidizing but less so than typical porphyry Mo-related silicic rocks (log FMQ = + 2 to + 3; Keith et al. 1993).

Comparison with Sn ± Nb-mineralized granites in the Nigerian alkaline province

Magma composition, redox state, and degree of fractionation exert fundamental controls on the propensity of granitic magmas to cause Mo or Sn mineralization (Blevin et al. 1996; Černý et al., 2005). The occurrence, in the Nigerian Mesozoic alkaline granite complexes, of Sn ± (Nb) and Mo mineralization implies that petrogenetic factors suitable for the formation of both styles of mineralization were involved in the generation of the alkaline granites during the Mesozoic (Kinnaird and Bowden 1987; Girei et al. 2019a, b). The Mo-mineralized granite from the Kigom Complex yielded a U/Pb
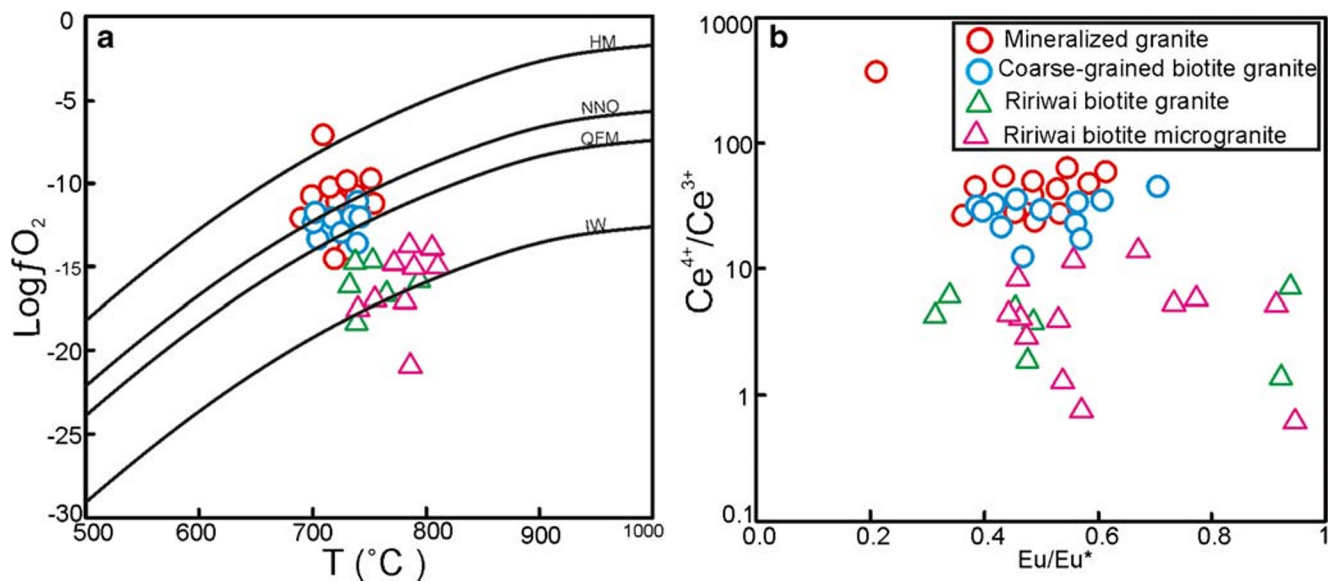
Fig. 10 **a** $\log fO_2$ versus T/°C for the Mada mineralized and coarse-grained biotite granites. **b** Ce^{4+}/Ce^{3+} versus Eu/Eu* for the Mada mineralized and coarse-grained biotite granites. All parameters were computed from zircon composition. Note: NNO = nickel-nickel oxide buffer, FQM = fayalite- quartz-magnetite buffer, Hm = hematite buffer, and IW = iron-wüstite buffer

age of 166 ± 4 Ma (Hafizullah Abba Ahmed, pers. comm., 2020), close to the whole-rock Rb-Sr age of the nearby Jos-Bukuru Sn ± (Nb)-mineralized ring complex (Rahaman et al. 1984), suggesting that Sn ± (Nb)- and Mo-mineralized granites are spatially and temporally related. However, unlike in the Mo-mineralized ring complexes, the intrusive sequence in the Sn ± (Nb)-mineralized ring complexes almost invariably commenced with the emplacement of fayalite-bearing granite porphyry, implying that their parental magmas were probably more reduced than those of the Mo-mineralized granite (Imeokparia 1985; Girei et al. 2019a, b). This is corroborated by the calculated fO_2 of the granite magma, which shows that Mo mineralization in the Mada Complex occurred under more oxidized conditions than Sn ± Nb mineralization in the Ririwai Complex (Fig. 10a–b).

A compilation of previous whole-rock data of aluminous granites associated with primary Sn ± Nb mineralization in the Ririwai and Tibchi ring complexes (Batchelor and Bowden 1986; Girei et al. 2019a, b), and of peralkaline granites associated with Mo mineralization in the Kigom Complex (Imeokparia 1985), together with our data, permits further comparisons between Mo- and Sn ± Nb-mineralized granites in Nigeria. Compared to the Mo-mineralized granites, the Sn± Nb-mineralized granites are more silicic and have higher Rb, higher Rb/Sr, larger Eu anomalies, and a higher differentiation (Thornton and Tuttle 1960) but lower Sr and Zr/Hf ratios, indicating that they are more fractionated than the Mo-mineralized granites (Fig. 11a–d). This is in broad agreement with the observation made by Blevin and Chappell (1995) in eastern Australia, where mineralization by chalcophile elements (Mo and Cu) was associated with less fractionated granites than mineralization by lithophile elements (Sn and Nb).

Comparison with other Mo-mineralized within-plate granites

Economically significant Mo mineralization associated with highly differentiated within-plate silicic alkaline rocks (i.e., A-type granites) has also been reported from many parts of the world, especially the western USA and eastern Qinling Mountains, China (Carten et al. 1993; Blevin 2004; Audétat and Li 2017). Compared to typical within-plate A-type suites containing porphyry Mo, such as the Climax-type Henderson deposits (CO, USA), the Mada and Kigom A-type granites have lower Rb concentrations (< 500 ppm) and Rb/Sr (< 30) and Nb/Zr (< 1) ratios (Carten et al. 1993; Keith et al. 1997; EMS 3 Fig. S3a-b). This suggests that the Mada and Kigom A-type granites are less differentiated than the A-type suite associated with the Henderson Mo deposits (Carten et al. 1993; Mercer et al. 2014). On the other hand, except for their higher Zr and Nb contents, the Mada and Kigom A-type granites share similar geochemical features with the Climax-type Questa deposits (NM, USA), which are regarded as a "transitional-type" Mo deposit (Carten et al. 1993; Rosera et al. 2013).

Genetic model

The whole-rock and zircon elemental data indicate that the Mada A-type granites are highly fractionated and have relatively high fO_2, characteristic features that collectively favored the formation of Mo mineralization (Černý et al., 2005; Audétat and Li 2017). In an oxidized aluminous melt, the concentration of Mo increases with increasing degree of magmatic differentiation prior to its final removal into
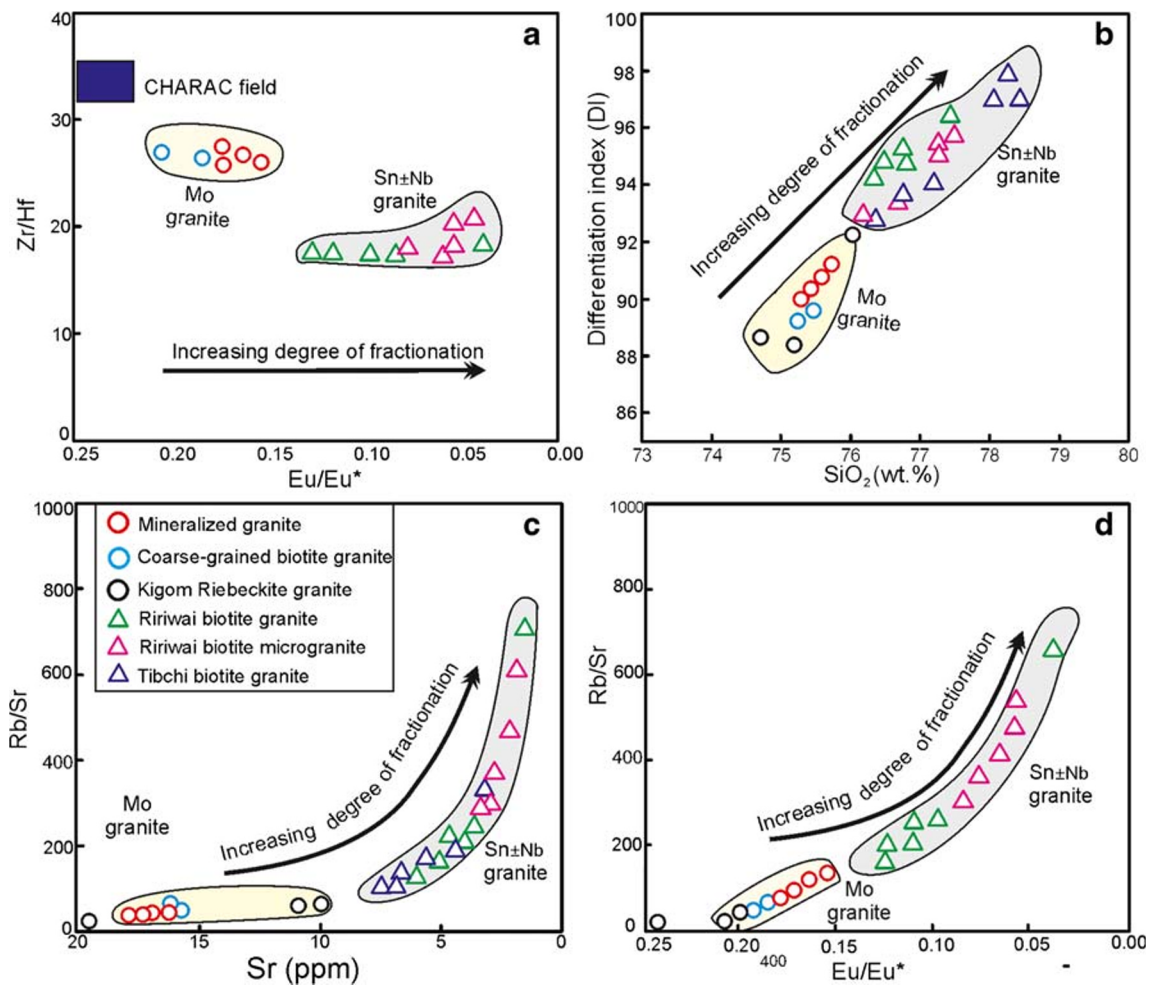
Fig. 11 **a** Plot of Zr/Hf versus Eu/Eu*. **b** Plot of differentiation index (DI) versus SiO₂. **c** Plot of Rb/Sr versus Sr. **d** Plot of Rb/Sr versus Eu/Eu*. Data plotted include those for Mo-mineralized granites from the Mada Complex (this study), and Kigom Complex (Imeokparia 1985), and Sn ± Nb-mineralized granites from the Ririwai Complex (Girei et al. 2019a, b)

and Tibchi Complex (Batchelor and Bowden 1986). Blue box indicates field of "normal" (unfractionated) granites that exhibit charge and radius controlled (CHARAC) behavior of HFSE (Zr, Hf) as defined by Bau (1996)
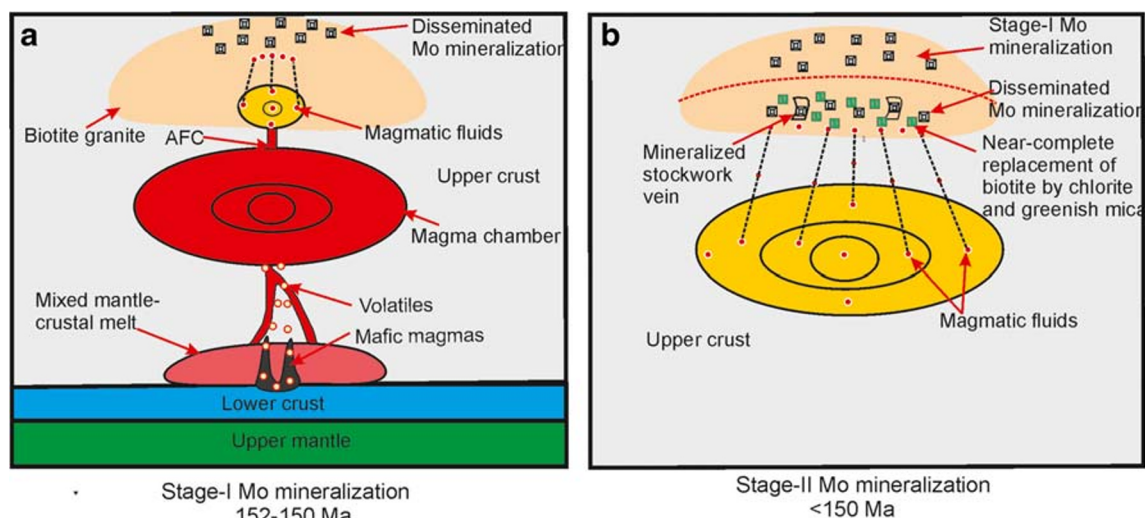

Fig. 12 Schematic diagram showing the two-staged molybdenum ore-forming event in the Mada Ring Complex. **a** Stage I. **b** Stage II. See text for detail explanation

exsolved ore-forming fluids at a late magmatic stage (Audétat and Li 2017). Previous studies have suggested that mafic magmas in a Climax-type mineralization system probably contribute significant amounts of volatiles (S and CO_2) and Mo to the mineralizing magmas through volatile fluxes (Keith et al. 1997; Audétat and Li 2017). Mafic rocks are present in the Mada Complex, and it is possible that their parental magmas, apart from contributing volatiles to the mineralizing magmas, may have also contributed heat that served to extend the lifetime of the magma chamber and enhanced the degree of fractional crystallization (Audétat and Li 2017; Zhang et al. 2018).

Molybdenum mineralization in the Mada Complex probably occurred in two separate stages (Figs. 3a–f, 12a–b). During Stage I, high-temperature potassic alteration was accompanied by deposition of disseminated Mo minerals (Fig. 12a). During Stage II, emplacement of greisen-related disseminated Mo mineralization with minor stockwork veins occurred, a process that was accompanied by near-complete replacement of biotite by chlorite and greenish mica due to fluid-rock interactions (Fig. 12b).

Conclusions

1. Integrated zircon U-Pb dating and molybdenite Re-Os systematics indicate that granite emplacement and Mo mineralization in the Mada Ring Complex of north-central Nigeria took place between 152 ± 1 and 150 ± 1 Ma, corresponding to the Late Jurassic.

2. Granites associated with Mo mineralization at Mada show elevated whole-rock concentrations of SiO_2, Nb, Zr, Y, and REEs (except Eu) and high $^{87}Rb/^{86}Sr$ ratios, but low concentrations of Sr, Ba, CaO, MgO, and TiO_2, typical of highly differentiated A-type granites. They yielded negative whole-rock $\varepsilon Nd(t)$ (-5.87 to -5.47) and zircon $\varepsilon Hf(t)$ (-4.97 to -10.06), indicating that both the A-type magma and Mo ore components were largely sourced from the lower crust with a contribution from the upper mantle.

3. Compared to their associated $Sn \pm (Nb)$-mineralized granites, the Mada A-type granites are less differentiated but have higher fO_2. These differences in redox state and degree of fractionation suggest that, despite their close temporal relationship, co-existing Mo- and $Sn \pm (Nb)$-mineralized A-type granites in the Nigerian alkaline province were probably derived from different source(s) and/or may have experienced contrasting evolutionary histories.

References

Abaa SI (1985) The structure and petrography of alkaline rocks of the Mada Younger Granite complex. Nigeria J African Earth Sci 3:107–113. https://doi.org/10.1016/0899-5362(85)90029-6

Ahmed HA, Ma C, Wang L, Palinkaš LA, Girei MB, Zhu Y, Habib M (2018) Petrogenesis and tectonic implications of peralkaline A-type granites and syenites from the Suizhou-Zaoyang region. Central China J Earth Sci 29:1881–1202. https://doi.org/10.1007/s12583-018-0877-2

Audétat A, Li W (2017) The genesis of climax-type porphyry Mo deposits: insights from fluid inclusions and melt inclusions. Ore Geol Rev 88:436–460. https://doi.org/10.1016/j.oregeorev.2017.05.018

Ballard JR, Palin JM, Campbell IH (2002) Relative oxidation states of magmas inferred from Ce"IV"/Ce"III" in zircon: application to porphyry copper deposits of northern Chile. Contrib Mineral Petrol 144:347–364. https://doi.org/10.1007/s00410-002-0402-5

Barra F, Deditius A, Reich M, Kilburn MR, Guagliardo P, Roberts MP (2017) Dissecting the Re-Os molybdenite geochronometer. Sci Rep 7:16054. https://doi.org/10.1038/s41598-017-16380-8

Barton IF (2019) Rhenium in molybdenite: a database approach to identifying geochemical controls on the distribution of a critical element. Min Metall Explor 37:21–37. https://doi.org/10.1007/s42461-019-00145-0

Batchelor RA, Bowden P (1986) Major and trace element analyses of volcanic and sub-volcanic igneous rocks from the Nigeria-Niger anorogenic province. Overseas development administration. Res Scheme Suppl Bull 2679:58

Bau M (1996) Controls on the fractionation of isovalent trace elements in magmatic and aqueous systems: evidence from Y/Ho, Zr/Hf and lanthanide tetrad effect. Contrib Mineral Petrol 123:323–333

Belousova EA, Griffin WL, O'Reilly SY (2006) Zircon crystal morphology, trace element signatures and Hf isotope composition as a tool for oetrogenetic modelling: examples from eastern Australian granitoids. J Petrol 47:329–353. https://doi.org/10.1093/petrology/egi077

Belousova EA, Griffin WL, O'Reilly SY, Fisher NI (2002) Igneous zircon: trace element composition as an indicator of source rock type. Contrib Mineral Petrol 143:602–622. https://doi.org/10.1007/s00410-002-0364-7

Berzina AP, Berzina AN, Gimon VO, Krymskii RS, Larionov AN, Nikolaeva IV, Serov PA (2013) The Shakhtama porphyry Mo ore-magmatic system (eastern Transbaikalia): age, sources, and genetic features. Russ Geol Geophys 54:587–605. https://doi.org/10.1016/j.rgg.2013.04.009

Berzina AN, Sotnikov VI, Economou-Eliopoulos M, Eliopoulos DG (2005) Distribution of rhenium in molybdenite from porphyry Cu-Mo and Mo-Cu deposits of Russia (Siberia) and Mongolia. Ore Geol Rev 26:91–113. https://doi.org/10.1016/j.oregeorev.2004.12.002

Blevin PL (2004) Redox and compositional parameters for interpreting the granitoid metallogeny of eastern Australia: implications for gold-rich ore systems. Resour Geol 54:241–252. https://doi.org/10.1111/j.1751-3928.2004.tb00205.x

Blevin PL, Chappell BW (1995) Chemistry, origin and evolution of mineralised granitoids in the LachlanFold Belt, Australia; the metallogeny of I- and S-type granitoids. Econ Geol 90:1604–1619

Blevin PL, Chappell BW, Allen CM (1996) On granite source and composition. Trans R Soc Edinb Earth Sci 87:281–290

Bonin B (2007) A-type granites and related rocks: evolution of a concept, problems and prospects. Lithos 97:1–29. https://doi.org/10.1016/j.lithos.2006.12.007

Bowden P (1985) The geochemistry and mineralization of alkaline ring complexes in Africa (a review). J Afr Earth Sci 3:17–39. https://doi.org/10.1016/0899-5362(85)90020-X

Bowden P, Black R, Martin RF, Ike EC, Kinnaird JA, Batchelor RA (1987) Niger-Nigerian alkaline ring complexes: a classic example of African Phanerozoic anorogenic mid-plate magmatism. Geol Soc Spec Publ 30:357–379. https://doi.org/10.1144/GSL.SP.1987.030.01.17

Bowden P, Kinnaird JA, Diehl M, Pirajno F (1990) Anorogenic granite evolution in Namibia—a fluid contribution. Geol J 25:381–390. https://doi.org/10.1002/gj.3350250320

Burnham AD, Berry AJ, Halse HR, Schofield PF, Cibin G, Mosselmans JFW (2015) The oxidation state of europium in silicate melts as a function of oxygen fugacity, composition and temperature. Chem Geol 411:248–259. https://doi.org/10.1016/j.chemgeo.2015.07.002

Bute SI, Yang X, Cao J, Liu L, Deng J, Vela Haruna I, Girei MB, Abubakar U, Akhtar S (2019) Origin and tectonic implications of ferroan alkali-calcic granitoids from the Hawal Massif, east-eastern Nigeria terrane: clues from geochemistry and zircon U-Pb-Hf isotopes. Int Geol Rev 62:129–152. https://doi.org/10.1080/00206814.2019.159325

Candela PA, Piccoli P (2005) Magmatic processes in the development of porphyry-type ore systems. Econ Geol 3:25–37. https://doi.org/10.5382/AV100.03

Carten RB, White WH, Stein HJ (1993) High-grade granite-related molybdenum systems: classification and origin. Geol Assoc Can Spec Pap 40:521–554

Christiansen EH, Keith JD (1996) Trace element systematics in silicic magmas: a metallogeneic prospective. Wyman DA (ed) Trace element geochemistry of volcanic rocks: applications for massive sulphide exploration. Geol. Assoc. Canada 12:115–151

Claiborne LL, Miller CF, Flanagan DM, Clynne MA, Wooden JL (2010) Zircon reveals protracted magma storage and recycling beneath Mount St. Helens Geol 38:1011–1014. https://doi.org/10.1130/G31285.1

Cooke DR, Agnew P, Hollings P, Baker M, Chang Z, Wilkinson JJ, Ahmed A, White NC, Zhang L, Thompson J, Gemmell JB, Chen H (2020) Recent advances in the application of mineral chemistry to exploration for porphyry copper–gold–molybdenum deposits: detecting the geochemical fingerprints and footprints of hypogene mineralization and alteration. Geochem: Explor, Environ, Anal 20:176–188. https://doi.org/10.1144/geochem2019-039

De la Roche H, Leterrier J, Grandclaude P, Marchal M (1980) A classification of volcanic and plutonic rocks using R-R2 diagram and major-element analyses–its relationships with current nomenclature. Chem Geol 29:183–210

Demaiffe D, Moreau C, Brown WL, Weis D (1991) Geochemical and isotopic (Sr, Nd and Pb) evidence on the origin of the anorthosite-bearing anorogenic complexes of the Aïr Province. Niger Earth Planet Sci Lett 105:28–46. https://doi.org/10.1016/0012-821X(91)90118-2

Dickin AP, Halliday AN, Bowden P (1991) A Pb, Sr and Nd isotope study of the basement and mesozoic ring complexes of the Jos Plateau. Nigeria Chem Geol 94:23–32. https://doi.org/10.1016/S0009-2541(10)80014-2

Ferry JM, Watson EB (2007) New thermodynamic models and revised calibrations for the Ti-in-zircon and Zr-in-rutile thermometers. Contrib Mineral Petrol 154:429–437. https://doi.org/10.1007/s00410-007-0201-0

Frost BR, Barnes CG, Collins WJ, Arculus RJ, Ellis DJ, Frost CD (2001) A geochemical classification for granitic rocks. J Petrol 42:2033–2048

Gaynor SP, Rosera JM, Coleman DS (2019) Intrusive history of the Oligocene Questa porphyry molybdenum deposit, New Mexico. Geosphere 15:548–575. https://doi.org/10.1130/GES01675.1

Girei MB, Li H, Algeo TJ, Bonin B, Ogunleye PO, Bute SI, Ahmed HA (2019a) Petrogenesis of A-type granites associated with Sn–Nb–Zn mineralization in Ririwai complex, north-Central Nigeria: constraints from whole-rock Sm-Nd and zircon Lu-Hf isotope systematics. Lithos 340–341:49–70. https://doi.org/10.1016/j.lithos.2019.05.003

Girei MB, Najime T, Ogunleye PO (2019b) Geochemical characteristics and origin of the Neoproterozoic high-K calc-alkaline granitoids in the northern part of Mandara hills, northeastern Nigeria. Acta Geochim. in press. https://doi.org/10.1007/s11631-019-00365-7

Imeokparia EB (1985) Geochemistry of intrusive rocks associated with molybdenum mineralization Kigom complex, northcentral Nigeria. Chem Geol 47:261–283

Jackson SE, Pearson NJ, Griffin WL, Belousova EA (2004) The application of laser ablation-inductively coupled plasma-mass spectrometry to in situ U–Pb zircon geochronology. Chem Geol 211:47–69

Jahn B, Wu F, Capdevila R, Martineau F, Zhao Z, Wang Y (2001) Highly evolved juvenile granites with tetrad REE pattern: the Woduhe and Baerzhe granites from the Great Xing'an mountains in NE China. Lithos 59:171–198

Jiang N (2005) Petrology and geochemistry of the Shuiquangou syenitic complex, northern margin of the North China Craton. J Geol Soc 162:203–215

Jiang WC, Li H, Evans NJ, Wu JH (2019) Zircon records multiple magmatic-hydrothermal processes at the giant Shizhuyuan W–Sn–Mo–Bi polymetallic deposit. South China Ore Geol Rev 115:1–22. https://doi.org/10.1016/j.oregeorev.2019.103160

Kamaunji VD, Wang LX, Ahmed HA, Zhu YX, Vincent VI, Girei MB (2020) Coexisting A1 and A2 granites of Kudaru complex: implications for genetic and tectonic diversity of A-type granite in the Younger Granite province, north-central Nigeria. Int J Earth Sci 109:511–535

Keith JD, Christiansen EH, Carten RB (1993) The genesis of giant porphyry molybdenum deposits. In: Whating BH, Mason R, Hodgson CJ (eds) Giant ore deposits. Society of Economic Geologists, special publication, vol 2, pp 285–317

Keith JD, Whitney JA, Hattori K, Ballantyne GH, Christiansen EH, Barr DL, Cannan TM, Hook CJ (1997) The role of magmatic sulfides and mafic alkaline magmas in the Bingham and Tintic mining districts. Utah J Petrol 38:1679–1690

Kerr A, Fryer BJ (1993) Nd isotope evidence for crust-mantle interaction in the generation of A-type granitoid suites in Labrador. Canada Chem Geol 104:1–4. https://doi.org/10.1016/0009-2541(93)90141-5

Kinnaird J, Bowden P (1987) African anorogenic alkaline magmatism and mineralization — a discussion with reference to the Niger-Nigerian Province. Geol J 22:297–334. https://doi.org/10.1002/gj.3350220622

Kinnaird JA, Bowden P, Ixer RA, Odling NWA (1985) Mineralogy, geochemistry and mineralization of the Ririwai complex, northern Nigeria. J Afr Earth Sci 3:185–222. https://doi.org/10.1016/0899-5362(85)90036-3

Kinnaird JA, Nex PAM, Milani L (2016) Tin in Africa. Episodes. 39:362–380. https://doi.org/10.18814/epiiugs/2016/v39i2/95783

Kirkland CL, Smithies RH, Taylor RJM, Evans N, McDonald B (2015) Zircon Th/U ratios in magmatic environs. Lithos. 212:397–414

Kirwin D (2012) Granite-related ore deposits. Econ Geol 107:383–384. https://doi.org/10.2113/econgeo.107.2.383

Klemm LM, Pettke T, Heinrich CA (2008) Fluid and source magma evolution of the Questa porphyry Mo deposit, New Mexico. USA Miner Depos 43:533–552. https://doi.org/10.1007/s00126-008-0181-7

Li J, Liang XR, Xu JF, Suzuki K, Dong YH (2010) Simplified technique for the measurements of Re-Os isotope by multicollector inductively coupled plasma mass spectrometry (MC-ICP-MS). Geochem J 44:73–80

Li H, Palinkaš LA, Evans NJ, Watanabe K (2019) Genesis of the Huangshaping W–Mo–Cu–Pb–Zn deposit, South China: role of magmatic water, metasomatized fluids, and basinal brines during intra-continental extension. Geol J 55:1409–1130. https://doi.org/10.1002/gj.3505

Li H, Palinkaš LA, Watanabe K, Xi XS (2018) Petrogenesis of Jurassic A-type granites associated with Cu-Mo and W-Sn deposits in the central Nanling region, South China: Relation to mantle upwelling and intra-continental extension. Ore Geol Rev 92:449–462. https://doi.org/10.1016/j.oregeorev.2017.11.029

Li H, Sun HS, Algeo TJ, Wu JH, Cao JY, Wu QH (2018) Mesozoic multi-stage W–Sn polymetallic mineralization in the Nanling range, South China: an example from the Dengfuxian–Xitian ore field. Geol J 54:3755–3785. https://doi.org/10.1002/gj.3369

Li H, Sun HS, Wu JH, Evans NJ, Xi XS, Peng NL, Cao JY, Gabo-Ratio JAS (2017) Re–Os and U–Pb geochronology of the Shazigou Mo polymetallic ore field, Inner Mongolia: implications for Permian–Triassic mineralization at the northern margin of the North China Craton. Ore Geol Rev 83:287–299. https://doi.org/10.1016/j.oregeorev.2016.12.010

Li H, Watanabe K, Yonezu K (2014) Zircon morphology, geochronology and trace element geochemistry of the granites from the Huangshaping polymetallic deposit, South China: implications for the magmatic evolution and mineralization processes. Ore Geol Rev 60:14–35. https://doi.org/10.1016/j.oregeorev.2013.12.009

Liu Y, Bagas L, Jiang S (2019) Genesis of porphyry Mo deposits linked to gradually dehydrating subcontinental lithospheric mantle metasomatised by previous subduction in northeastern China. Lithos 336–337:143–150. https://doi.org/10.1016/j.lithos.2019.03.035

Liu YS, Hu ZC, Zong KQ, Gao CG, Gao S, Xu J, Chen HH (2010) Reappraisement and refinement of zircon U-Pb isotope and trace element analyses by LA-ICP-MS. Chin Sci Bull 55:1535–1546

Lowenstern JB, Sinclair WD (1996) Exsolved magmatic fluid and its role in the formation of comb-layered quartz at the Cretaceous Logtung W-Mo deposit, Yukon territory. Canada Spec Pap Geol Soc Am 315:291–303. https://doi.org/10.1130/0-8137-2315-9.291

Machado N, Simonetti A (2001) U–Pb dating and Hf isotopic composition of zircon by laser ablation MC-ICP-MS. In: Sylvester P (ed) Principles and Applications of Laser-Ablation ICP-Mass Spectrometry in the Earth Sciences, Mineralogical Association of Canada, Short Course, vol 29, pp 121–146

Magaji SS, Martin RF, Ike EC, Ikpokonte AE (2011) The Geshere syenite-peralkaline granite pluton: a key to understanding the anorogenic Nigerian Younger Granites and analogues elsewhere. Period di Mineral 80:199–213. https://doi.org/10.2451/2011PM0016

Mao JW, Pirajno F, Lehmann B, Berzina A (2014) Distribution of porphyry deposits in the Eurasian continent and their corresponding tectonic settings. J Asia Earth Sci 79:576–584

Mao JW, Wang YT, Lehmann B, Yu JJ, Du AD, Mei YX, Li YF, Zang WS, Stein HJ, Zhou TF (2006) Molybdenite Re–Os and albite 40Ar/39Ar dating of Cu–Au–Mo and magnetite porphyry systems in the Changjiang valley and metallogenic implications. Ore Geol Rev 29:307–324

Mao J, Zhaochong Z, Zuoheng Z, Andao D (1999) Re-Os isotopic dating of molybdenites in the Xiaoliugou W (Mo) deposit in the northern Qilian mountains and its geological significance. Geochim Cosmochim Acta 63:1815–1818. https://doi.org/10.1016/S0016-7037(99)00165-9

Martin RF, Sokolov M, Magaji SS (2012) Punctuated anorogenic magmatism. Lithos 152:132–140. https://doi.org/10.1016/j.lithos.2012.05.020

Mercer CN, Hofstra AH, Todorov TI, Roberge J, Burgisser A, Adams DT, Cosca M (2014) Pre-eruptive conditions of the hideaway park topaz rhyolite: insights into metal source and evolution of magma parental to the Henderson porphyry molybdenum deposit. Colorado J Petrol 56:645–679. https://doi.org/10.1093/petrology/egv010

Miller JS, Matzel JEP, Miller CF, Burgess SD, Miller RB (2007) Zircon growth and recycling during the assembly of large, composite arc plutons. J Volcanol Geotherm Res 167:282–299. https://doi.org/10.1016/j.jvolgeores.2007.04.019

Moreau C, Demaiffe D, Bellion Y, Boullier AM (1994) A tectonic model for the location of Palaeozoic ring complexes in Aïr (Niger, West Africa). Tectonophysics 234:129–146. https://doi.org/10.1016/0040-1951(94)90208-9

Ngako V, Njonfang E, Aka FT, Affaton P, Nnange JM (2006) The north-south Paleozoic to Quaternary trend of alkaline magmatism from Niger-Nigeria to Cameroon: complex interaction between hotspots and Precambrian faults. J Afr Earth Sci 45:241–256. https://doi.org/10.1016/j.jafrearsci.2006.03.003

Ouyang H, Mao J, Hu R (2020) Geochemistry and crystallization conditions of magmas related to porphyry Mo mineralization in northeastern China. Econ Geol 115:79–100

Pastor J, Turaki UM (1985) Primary mineralization in Nigerian ring complexes and its economic significance. J Afr Earth Sci 3:223–227. https://doi.org/10.1016/0899-5362(85)90037-5

Pearce JA, Harris NW, Tindle AG (1984) Trace element discrimination diagrams for the tectonic interpretation of granitic rocks. J Petrol 25:956–9

Pettke T, Oberli F, Heinrich CA (2010) The magma and metal source of giant porphyry-type ore deposits, based on lead isotope microanalysis of individual fluid inclusions. Earth Planet Sci Lett 296:267–277. https://doi.org/10.1016/j.epsl.2010.05.007

Poitrasson F, Duthou JL, Pin C (1995) The relationship between petrology and Nd isotopes as evidence for contrasting anorogenic granite genesis: example of the corsican province (SE France). J Petrol 36:1251–1274. https://doi.org/10.1093/petrology/36.5.1251

Rahaman MA, Van Breemen O, Bowden P, Bennett JN (1984) Age migration of anorogenic ring-complexes in northern Nigeria. J Geol 92:173–184

Rosera JM, Coleman DS, Stein HJ (2013) Re-evaluating genetic models for porphyry Mo mineralization at Questa, New Mexico: implications for ore deposition following silicic ignimbrite eruption. Geochem Geophys Geosyst 14:787–805. https://doi.org/10.1002/ggge.20048

Schiller D, Finger F (2019) Application of Ti-in-zircon thermometry to granite studies: problems and possible solutions. Contrib Mineral Petrol 174:1–16. https://doi.org/10.1007/s00410-019-1585-3

Selby D, Creaser RA, Heaman LM, Hart CJR (2003) Re-Os and U–Pb geochronology of the Clear Creek, Dublin Gulch, and Mactung deposits, Tombstone Gold Belt, Yukon, Canada: absolute timing relationships between plutonism and mineralization. Can J Earth Sci 40:1839–1852. https://doi.org/10.1139/E03-077

Shand SJ (1943) Eruptive rocks: their genesis, composition, classification, and their relation to ore-deposits, with a chapter on meteorites. John Wiley & Sons, New York, 350 pp

Siégel C, Bryan SE, Allen CM, Gust DA (2018) Use and abuse of zircon-based thermometers: a critical review and a recommended approach to identify antecrystic zircons. Earth-Sci Rev 176:87–116. https://doi.org/10.1016/j.earscirev.2017.08.011

Slama J, Kosler J, Condon DJ, Crowley JL, Gerdes A, Hanchar JM, Horstwood MSA, Morris GA, Nasdala L, Norberg N, Schaltegger U, Schoene N, Tubrett MN, Whitehouse MJ (2008) Plesovice zircon

- a new natural reference material for U-Pb and Hf isotopic micro-analysis. Chem Geol 249:1–35

Smoliar MI, Walker RJ, Morgan JW (1996) Re-Os ages of group IIA, IIIA, IVA, and IVB iron meteorites. Science 271:1099–1102

Smythe DJ, Brenan JM (2016) Magmatic oxygen fugacity estimated using zircon-melt partitioning of cerium. Earth Planet Sci Lett 53:260–266

Stein HJ (2006) Low-rhenium molybdenite by metamorphism in northern Sweden: recognition, genesis, and global implications. Lithos 87:300–327. https://doi.org/10.1016/j.lithos.2005.06.014

Stein HJ (2013) Dating and tracing the history of ore formation. In: Holland HD, Turekian KK (eds) Treatise on Geochemistry, vol 13, 2nd edn, pp 87–118. https://doi.org/10.1016/B978-0-08-095975-7.01104-9

Stein HJ, Hannah J (1985) Movement and origin of ore fluids in climax-type systems. Geology 13:469–474. https://doi.org/10.1130/0091-7613(1985)13<469:MAOOOF>2.0.CO;2

Stein HJ, Markey RJ, Morgan JW, Hannah JL, Scherstén A (2001) The remarkable Re-Os chronometer in molybdenite: how and why it works. Terra Nova 13:479–486. https://doi.org/10.1046/j.1365-3121.2001.00395.x

Stein HJ, Sundblad K, Markey RJ, Morgan JW, Motuza G (1998) Re±Os ages for Archaean molybdenite and pyrite, Kuittila-Kivisuo, Finland and Proterozoic molybdenite,Kabeliai, Lithuania: testing the chronometer in a metamorphic and metasomatic setting. Mineral Deposita 33:329–345

Sun W, Huang R-F, Li H, Hu Y-b, Zhang C-c, Sun S-j, Zhang L-p, Ding X, Li C-y, Zartman RE, Ling M-x (2015) Porphyry deposits and oxidized magmas. Ore Geol Rev 65:97–131. https://doi.org/10.1016/j.oregeorev.2014.09.004

Suzuki K, Feely M, O'relly C (2001) Disturbance of the Re-Os chronometer of molybdenites from the late-Caledonian Galway granite, Ireland, by hydrothermal fluid circulation. Geochem J 35:29–35

Thornton CP, Tuttle OF (1960) Chemistry of igneous rocks. I Differentiation index. Am J Sci 258:664–684

Trail D, Bruce Watson E, Tailby ND (2012) Ce and Eu anomalies in zircon as proxies for the oxidation state of magmas. Geochim Cosmochim Acta 97:70–87. https://doi.org/10.1016/j.gca.2012.08.032

Villaseca C, Barbero L, Rogers G (1998) Crustal origin of Hercynian peraluminous granitic batholiths of central Spain: petrological, geochemical and isotopic (Sr, Nd) constraints. Lithos 43:55–79

Walraven F, Strydom JH, Strydom N (1990) Rb-Sr open system behaviour and its application as a pathfinder for Sn mineralisation in granites of the Bushveld complex, South Africa. J Geochem Explor 37:333–350

Wanhainen C, Nigatu W, Selby D, McLeod CL, Nordin R, Bolin NJ (2014) The distribution, character, and rhenium content of molybdenite in the Aitik Cu-Au-Ag-(Mo) deposit and its southern extension in the northern Norrbotten Ore District, northern Sweden. Minerals 4:788–814. https://doi.org/10.3390/min4040788

Watson EB, Harrison TM (1983) Zircon saturation revisited temperature and composition effects in a variety of crustal magma types. Earth Planet Sci Lett 64:295–304

Wu JH, Li H, Algeo TJ, Jiang WC, Zhou ZK (2018) Genesis of the Xianghualing Sn–Pb–Zn deposit, South China: a multi-method zircon study. Ore Geol Rev 102:220–239. https://doi.org/10.1016/j.oregeorev.2018.09.005

Yakymchuk C (2019) On granites. J Geol Soc India 94:9–22. https://doi.org/10.1007/s12594-019-1261-2

Zhai D, Williams-Jones AE, Liu J, Selby D, Li C (2019) Evaluating the use of the molybdenite Re-Os chronometer in dating gold mineralization: evidence from the Haigou deposit, northeastern China. Econ Geol 114:897–915. https://doi.org/10.5382/econgeo.4667

Zhang XJ, Lentz DR, Yao CL, Liu R, Yang Z, Mei YX, Fan XW, Huang F, Qin Y, Zhang K, Zhang Z (2018) Geochronology, geochemistry, and Sr–Nd–Pb–Hf isotopes of the Zhunsujihua granitoid intrusions associated with the molybdenum deposit, northern Inner Mongolia, China: Implications for petrogenesis and tectonicsetting. Int J Earth Sci 2018(107):687–710